
Categorical Distributions are Effective Neural Network Outputs for Event Prediction

Kevin Doran

Sussex Neuroscience
School of Engineering and Informatics
University of Sussex, UK
k.a.doran@sussex.ac.uk

Tom Baden

Sussex Neuroscience
School of Life Sciences
University of Sussex, UK
t.baden@sussex.ac.uk

Abstract

We demonstrate the effectiveness of using a simple neural network output, a categorical probability distribution, for the task of next spike prediction. This case study motivates an investigation into why this simple output structure is not commonly used with neural temporal point process models. We find evidence that many existing datasets for evaluating temporal point process models do not reveal much information about the underlying event generating processes, and many existing models perform well due to regularization effects of model size and constraints on output structure. We extend existing datasets and create new ones in order to explore outside of this information limited regime and find that outputting a simple categorical distribution is competitive across a wide range of datasets.

1 Introduction

Probabilistic modelling of event data with neural networks is the concern of the field of neural network based temporal point processes (TPPs), reviewed by Shchur et al. [2021], Bosser and Taieb [2023] and Lin et al. [2025].

Bosser and Taieb [2023] and Lin et al. [2025] catalogued performance differences of many neural TPP models but did not find an explanation for these differences. In this work, we identify properties of commonly used datasets that can explain performance differences between existing models. We extend the training set sizes of these datasets beyond those commonly used and find evidence that many existing models perform well due to regularization effects of model size and constraints on output structure. We observe datasets quickly plateau in terms of how much information they reveal about the underlying event generating process, explaining the success of smaller models. To explore model behaviour outside this information limited regime, we design new event processes with graded decoding difficulties, and with them observe the benefit of larger models being trained on larger training sets. Notably, we find evidence that, as a neural network output, a categorical distribution is competitive across a large proportion of the dataset landscape. The evidence supports the claim that properties of existing datasets have led to larger models paired with unconstrained outputs like the categorical distribution to be overlooked despite their effectiveness.

The above investigation was motivated by experience using TPP models to predict spike times of retinal ganglion cells. The details of this task are described in this work; this is done to introduce a new application motivated task for TPP models and to motivate the use of the categorical output.

Section 2 describes the spike prediction task. Section 3 covers the poor results of applying the categorical output to existing datasets. Section 4 extends the training set sizes and compares various models. Section 5 and Section 6 introduce new synthetic datasets that allow model performance to be explored outside the information limited regime and shed further light on characteristics of existing datasets.

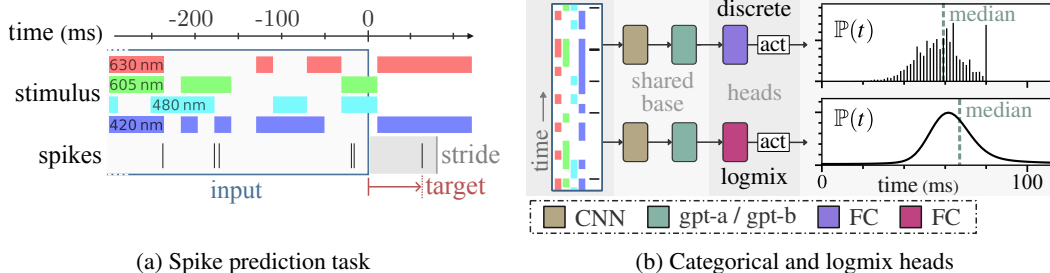


Figure 1: **(a)** Spike prediction task: given a 1-second snippet of stimulus and spike history, predict the time of the next spike. Predictions beyond a stride of 80 ms are not used. The 4-waveband stimulus and the spike times are recorded at a sample rate of 992 Hz. Information after $t = 0$ is not available to a model, matching the task faced by retinal prosthetic devices. **(b)** The inputs, architecture and outputs of two models tested at spike prediction. Figure adapted from Doran et al. [2024].

2 A categorical output is effective for spike prediction

Here we show that a spike prediction task is naturally served by a model with a simple output: an array of numbers representing a discrete probability distribution. This output is compared to using a lognormal mixture distribution investigated by Shchur et al. [2020], which we refer to as *logmix*.

We design a spike prediction task motivated by retinal prosthetic devices. Such devices must mimic the activity patterns of cells by considering impinging light and previous spike activity; for example, Gogliettino et al. [2023] tackles this problem in the primate retina. Using the same procedure as Doran et al. [2024], we create a dataset of snippets for 60 retinal ganglion cells (RGCs) from a multi-electrode array recording of a chicken retina [Seifert et al., 2023]. Each snippet has two parts: 1024 samples (~ 1 second) of stimulus and spike history as input, and the time until the next spike as output. Snippets contain activity of a single cell. A truncated snippet is shown in Figure 1a. We train two architectures (with a common base) using negative log-likelihood (NLL) loss. Point estimates are made using the median of the output distribution. To gauge how well models might operate in a retinal prosthetic device, we roll out the models autoregressively and compare the generated spike trains to the ground truth spike train using common spike train similarity metrics. The output heads and the shared base architecture are described next. The experiment and results follow in Section 2.4.

2.1 Motivating the categorical distribution head

Two temporal scales associated with the task make the use of a discrete probability mass output a natural choice: the sampling period and the prediction period. The *sampling period* of the spikes and stimulus is ~ 1 ms (1.008 ms). The autoregressive regime introduces the *prediction period*—the maximum duration to wait before making a new prediction. A shorter prediction period allows for faster integration of new stimulus information, but carries a computational cost. We fix 80 samples (~ 80 ms) as the prediction period. There are diminishing returns to reducing this period, as 80 ms is close to the mean response delay of the RGCs recorded by Seifert et al. [2023]. With 80 ms prediction period and 1 ms sampling period, an unconstrained and fully descriptive neural network output is 81 softmaxed numbers representing the probability of a spike occurring in 81 intervals: 80 intervals in the prediction period plus the interval $[80 \text{ ms}, \infty)$. No finer resolution than 1 ms is needed, and no granularity at all is needed beyond the 80 ms prediction period. The model output is depicted in the top right of Figure 1b above the output head it is compared against, the mixture of lognormals, which will be described next.

2.2 Mixture of lognormals head

Preliminary experiments with existing TPP approaches, many of which appear in Sections 4 to 6, highlighted the logmix output head, a mixture of lognormals investigated by Shchur et al. [2020], as an effective output structure for spike prediction. It is used in this work with 16 mixture components. Preliminary experiments revealed no benefit in using more components. An example output from a trained model is shown in the bottom right of Figure 1b.

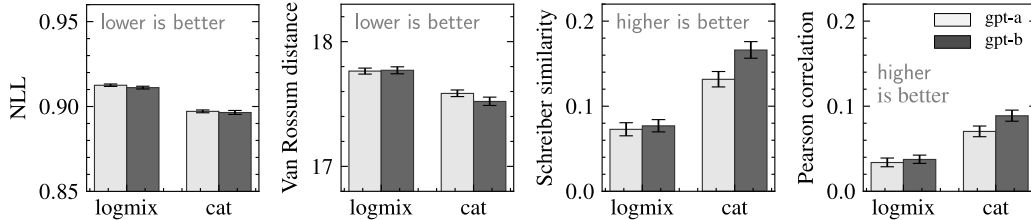


Figure 2: Performance comparison between two neural network outputs for spike prediction: *logmix* (a 16-component lognormal mixture distribution) and *cat* (an 81-bin probability mass function). Negative log-likelihood (NLL) is reported on the left. The next 3 metrics are spike train similarity/distance metrics, evaluated autoregressively; they share a smoothing parameter of 60 ms. The shared base architecture is tested in two sizes: *gpt-a* and a larger *gpt-b*. We follow the recommendation of Agarwal et al. [2021] and report metrics as interquartile means over the 60 chicken RGCs over 10 training repeats, with 95% bootstrap confidence intervals as error bars.

2.3 Shared base architecture: CNN + transformer (*gpt-a* and larger *gpt-b*)

Both the categorical and *logmix* output heads are attached to the same architecture: a convolutional neural network (CNN) followed by a transformer. A straightforward ResNet [He et al., 2016] based CNN stem encodes a 1024-length frame of stimulus and spike history into a 64-length sequence of vectors of length 64. This sequence is input to a small GPT-2 [Radford et al., 2019] transformer, denoted *gpt-a*, with 2 layers, 4 heads and an embedding size of 16. An embedding of the cell number (0–59) is added to the input sequence. The output of the transformer is either an 81 length vector in the case of the categorical output, or a $16 \times 3 = 48$ length vector in the case of the mixture of 16 lognormals. A second larger GPT-2 is also tested, with 6 layers, 4 heads and an embedding size of 32—this is denoted as *gpt-b*. Both *gpt-a* and *gpt-b* are also used in the experiments of Sections 4 to 6. Appendix D describes the CNN and transformer architectures in more detail.

2.4 Experiment and results

We train 4 models: the *logmix* and categorical heads with both *gpt-a* and *gpt-b* transformer variants. The models are trained at next spike prediction with an NLL loss (see Appendix B for training details). Point estimates are made using the median of the output distribution. We evaluate model performance with 4 metrics: NLL, Schreiber Similarity, Van Rossum distance and smoothed Pearson correlation. The latter 3 metrics are calculated using the spike trains generated by rolling out the models autoregressively; the metrics share a smoothing parameter set to 60 ms, a duration shown to be appropriate by Doran et al. [2024]. Schreiber similarity introduced by Schreiber et al. [2003] and Van Rossum distance introduced by Van Rossum [2001] are common metrics used to compare spike trains. See [Paiva et al., 2010] for a review of different spike train comparison metrics. The NLL calculation uses probability mass, and for the *logmix* model, this involves integrating the continuous distribution over a 1 ms interval.

All 4 metrics are reported in Figure 2. These results are expanded in Appendix B by considering an additional non-probabilistic output, the spike distance function introduced by Doran et al. [2024].

2.5 Discussion

Figure 2 captures two results. First, the model with a categorical output consistently outperforms the mixture of lognormals, highlighting the effectiveness of the simple output structure. Second, increasing the transformer size from *gpt-a* to *gpt-b* has neutral to positive effects. These results raise two questions. Firstly, the categorical output structure is effective at at least one TPP task; is it effective more broadly? Secondly, do other output heads benefit from being used with larger models? The remainder of this work follows from these questions. Existing datasets will be shown to not benefit from using the categorical output nor from larger models, but when these datasets are extended and new datasets are considered, the effectiveness of larger models and of the categorical output is revealed.

3 Mixed results on synthetic datasets from [Omi et al., 2019]

To test if the categorical distribution output is effective in other settings, we adapt it to work with continuous data and apply it to the synthetic datasets introduced by Omi et al. [2019].

The processes generating these datasets produce next event times in the range $(0, \infty)$. We interpret the categorical output as assigning probability mass to intervals. We follow a similar approach to Kvamme and Borgan [2021] and choose intervals that equally divide the training set distribution: we fix 128 intervals, choosing interval lengths such that the first interval extends to contain the first $1/128$ of the inter-event times, the second until $2/128$, and so on until the last interval which extends to infinity. We let the probability density in each interval be constant, determined by its fixed width and the model’s output. The last interval, being infinite in length, cannot have a constant non-zero density; instead we use an exponential decay weighted by the model’s output. Appendix D covers this in more detail. The bins for a model with 128 outputs when the training set is from a stationary Poisson process are shown in Figure 3.

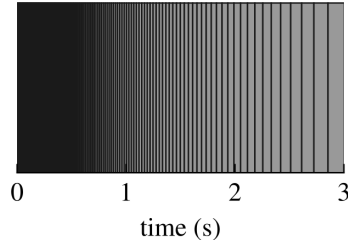


Figure 3: Bins for a model with 128 outputs when the training set is from a stationary Poisson process with a mean of 1 second.

Table 1 shows the results of `gpt-a-cat`, whose output is reinterpreted as above, and `gpt-a-logmix` applied to the synthetic datasets from [Omi et al., 2019]. The recurrent neural network (RNN) used by Shchur et al. [2020] when they introduced the `logmix` head is also included, which we denote as `rnn-logmix`. At first glance, the results are not encouraging for the categorical approach: on 4 of the 7 datasets it performs worse than `rnn-logmix`. However, what sets `rnn-logmix` apart is not the `logmix` head, but the small RNN base model, as `gpt-a-logmix` also performs notably worse than `rnn-logmix`. One reason for the competitiveness of small models can be that they are operating in a data limited regime and benefiting from the regularization effect of lower model capacity. We can understand if this is a cause by increasing the amount of training data. We explore this next.

Table 1: Three models evaluated in terms of test set NLL (lower is better) on 7 datasets generated following Omi et al. [2019]. Results for the `gpt` variants are reported by their difference to the results for `rnn-logmix`. Values are the mean over 10 trials (training with 10 datasets generated with different random number generator seeds). The number of trainable parameters for each model are listed in the second column. The table is expanded with variability information in Appendix A.

Model	Params	Poisson	Poisson (NS)	Self-correcting	Renewal	Renewal (NS)	Hawkes1	Hawkes2
<code>rnn-logmix</code>	29k	1.000	0.722	0.804	0.248	0.379	0.448	-0.0103
<code>gpt-a-logmix</code>	111k	+0.000	-0.027	-0.042	+0.000	-0.033	+0.004	+0.0049
<code>gpt-a-cat</code>	116k	+0.004	-0.012	-0.032	+0.006	-0.017	+0.019	+0.0283

4 Training set sizes differentiate TPP model performance

We extend the previous section’s experiment with additional models, additional datasets and with a range of training set sizes. The four models listed in Table 2 are included. To test the effects of increasing model capacity, the output heads of the RNN models are also attached to the `gpt-a` transformer introduced in Section 2. The Transformer Hawkes model is already described by Zuo et al. [2020] in two sizes, which we refer to as `thp-0` and `thp-1`.

In addition to the 7 synthetic datasets, we evaluate models on sequences of taxi pickup times in New York City [Whong, 2014, Du et al., 2016] and badge reward times on the site Stack Overflow [Du et al., 2016]. The training set of all datasets is varied across 16 sizes from 2^{10} to 2^{25} inter-event times. The validation and test sets are fixed, with 2^{17} inter-event times in each. None of the 15 datasets used by Bosser and Taieb [2023] nor any of the datasets from Xue et al. [2023] have sufficient event counts to be used across this range of training set sizes. The NYC taxi and Stack Overflow badge datasets were chosen as they could be recreated from the original data sources to be large enough to support these larger training sets (see Appendix C). The next section covers the results of this experiment.

Table 2: Four models used in experiments. Implementation details are described in Appendix D.

Label	Model stem	Head output	Studied by
rnn-const	RNN	exponential hazard	Huang et al. [2019], Li et al. [2018]
rnn-exp	RNN	constant hazard	Du et al. [2016]
rnn-nn	RNN	neural net parameterized hazard	Omi et al. [2019]
thp	transformer	softplus hazard	Zuo et al. [2020]

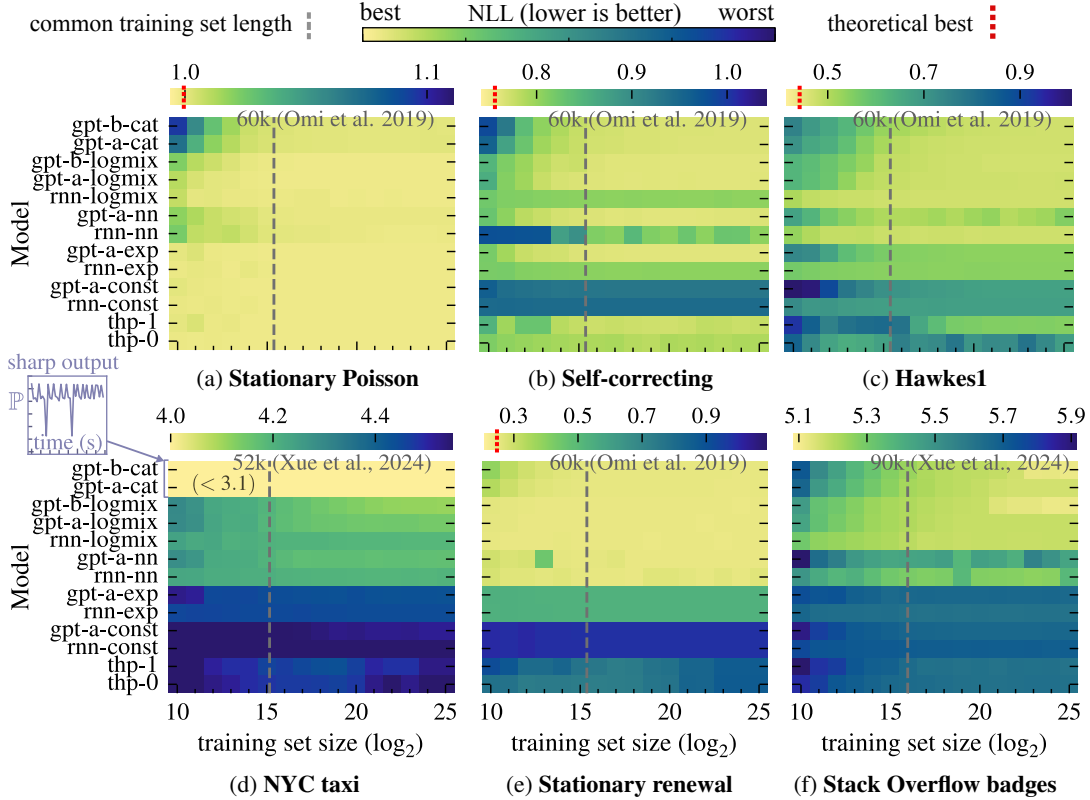


Figure 4: Performance comparison of 13 models in terms of test set NLL across 6 datasets and 16 training set lengths from 2^{10} to 2^{25} . The colormap ranges span each sub-figure’s full range of values, except for the NYC taxi dataset, where the categorical models’ very low NLL scores (all < 3.1) are separated to preserve the colormap detail for the other models. For synthetic datasets where a theoretical best score is known, it is marked with a red dashed line.

4.1 Results and discussion

Figure 4 reports NLL for all models on 6 datasets. Appendix A contains the complete results (NLL and mean absolute error (MAE) for all datasets). The results support three claims: first, that training set size is an important factor in explaining performance; second, that with more data, the synthetic datasets do not reveal much additional information about the underlying event generating processes; finally, that the discrete nature of real-world data should be considered when designing and evaluating models.

The training set length has a significant effect on the rank of the models in terms of performance. For most of the datasets, the larger models take more samples to plateau but eventually catch up to or surpass their smaller counterparts. In particular, the poorer scores observed for gpt-a-logmix and gpt-a-cat in Section 3 are dependent on training set size and diminish as sizes increase.

A striking observation is that for all synthetic datasets there is a model that requires very little data to be a top-scoring model. We argue that this is evidence that the datasets quickly reach a ceiling in terms

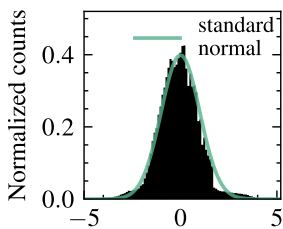


Figure 5: Histogram of 200k samples from the modified Metropolis-Hastings algorithm.

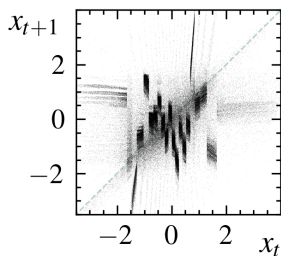


Figure 6: 200k pairs of samples rasterized: x_{t+1} and previous sample x_t .

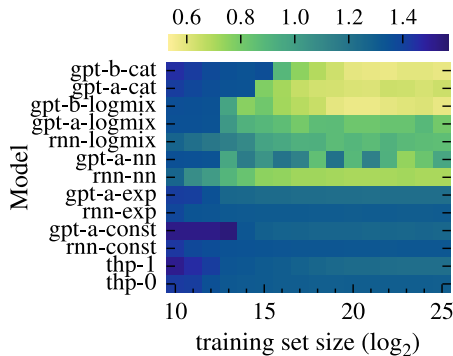


Figure 7: NLL scores for all models on the Metropolis lognormal dataset.

of how much information they reveal about the underlying event generating process. Take for example the stationary Poisson process where, after a few thousand samples, most of the models tested have reached close to the theoretical best NLL score, and pushing beyond this would involve inferring the state of the underlying pseudo-random number generator. In the next section we introduce a new synthetic dataset that provides more usable information over longer training lengths.

The final observation pertains to the NYC taxi dataset. For this dataset, both categorical models obtained very low NLL values across all training set lengths. The models’ outputs contained many high densities in intervals a few seconds wide. This highlights the importance of admitting the discrete nature of most real-world data and the importance of specifying the resolution of interest, for example, minutes or hours, as was done with the spike prediction task.

5 Metropolis lognormal event dataset

We created a synthetic dataset where small models do not reach competitive performance on small training sets. A hypothesis is that if the generating process has various levels of state inferable with different amounts of data, then models will benefit from being trained on larger training sets. To achieve this, we generate an event sequence from a nested set of state transition matrices. The matrices are used within a modified Metropolis-Hastings sampling algorithm. This process exploits what is typically considered a weakness of Metropolis-Hastings sampling—that samples are dependent—in order to gradually leak information about the underlying state transition matrices, all while generating a sequence with an ostensibly lognormal inter-event distribution. In the next section, we give an overview of the event generation procedure. The same models from the previous section are retrained on this dataset, and the results are described in Section 5.2.

5.1 Sequence generation

A sequence is generated as follows. First, a transition matrix that defines a cycle between states is fixed. We use 20 states (shown in Appendix C.3). The domain, $(-\infty, \infty)$, is split into 22 bins: two outer bins, $(-\infty, 4.3)$ and $(4.3, \infty)$, which each contain a small amount (10^{-5}) of the probability mass of a normal distribution, and 20 bins that share the remaining (>99%) probability mass evenly. The Metropolis-Hastings sampling process uses a proposal distribution located at the previous sample. We modify this process to first follow the transition matrix to a new state before sampling with a proposal distribution from the corresponding location in the new interval. We nest this process by having the proposal distribution also be a pseudo-normal distribution generated by the same process but with a separate transition matrix. The log of the generated values become a sequence of inter-event times. Appendix C.3 explains the sampling process in more detail. Figure 5 plots samples from the sequence before taking the log, revealing the roughly Gaussian shape of the distribution. For the same samples, Figure 6 plots next vs. previous samples, highlighting that with enough samples, a highly structured distribution emerges.

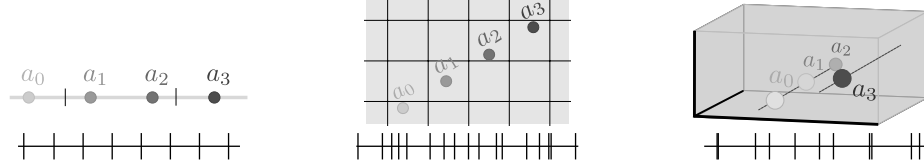


Figure 8: Four snapshots of a particle moving in 1, 2 and 3-dimensional space. When the particle passes a boundary, an event is generated. An example event sequence is shown. The 3-dimensional case is visualized by the particle wrapping around in a single voxel.

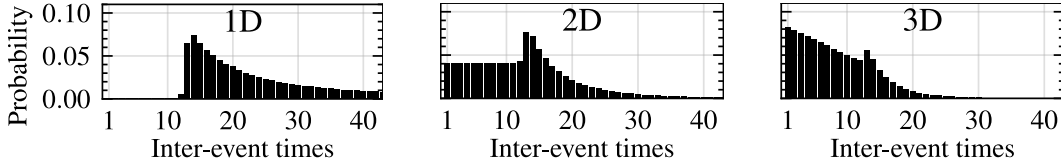


Figure 9: Inter-event time distributions for 1, 2 and 3-d modulo sequences where the starting position, a_0 , is sampled uniformly from $[0, 1021)^d$ and the velocity, v , uniformly from $[10, 80]^d$.

5.2 Results and discussion

Figure 7 shows how models perform across a range of training set lengths. Here, all heads (except `nn`) benefit from having a larger base model, and smaller models do not quickly approach a competitive score. This dataset is important for being a synthetic event based dataset where there is a clear benefit of using larger models, and those models gradually improve with more data. Regarding the `nn` head, we note that for previous datasets too, like Stack Overflow badges, `gpt-a-nn` performs poorly relative to `rnn-nn`; we observed `gpt-a-nn` to be more prone to training instability compared to `rnn-nn`.

The next section creates a family of event processes in order to identify relationships between decoding difficulty, usable information and the performance of various model output structures.

6 Event sequences from modulo addition

An increasing sequence defined over a grid can be used to generate event sequences with varying degrees of complexity. Consider tracking a particle along a 1D track and recording when the particle passes 10 meters, 20 meters, 30 meters and so on. Over a 2D plane, we could record the times when a particle moves from one quadrant to another. As the number of dimensions increases, the number of faces a particle can exit through to enter another division increases. Figure 9 shows a particle moving in 1D, 2D and 3D space and generating events with respect to a grid. To predict when a particle will move to the next quadrant, the previous events can be observed to narrow down the particle’s position and velocity. This becomes more challenging and requires more data points as the number of dimensions increases. By varying the number of dimensions, a family of event sequences can be created with various difficulties and data requirements, and this can be used to characterize performance of event prediction models and indirectly characterize other datasets.

6.1 10 datasets, from 1D to 10D

We create 10 datasets of *discrete time* event sequences, one for each dimension from 1 to 10. Discrete rather than continuous event times are chosen so as to return to the original setting seen in the spike prediction task (it also reflects the discrete nature of the NYC taxi and Stack Overflow datasets).

A 1-dimensional sequence is generated as follows. A grid size n is fixed. In this work, we use $n = 1021$. A velocity v and starting position a_0 are chosen. A sequence of positions a_0, a_1, a_2, \dots is generated by $a_{i+1} = a_i + v$. Whenever $a_{i+1} < a_i \bmod n$, an event is generated at time $t = i + 1$.

A d-dimensional sequence is generated from *vector* addition in the same way. A vector \mathbf{n} of length d is fixed. We fix \mathbf{n} to be $\mathbf{n} = (1021, 1021, \dots, 1021)$. A velocity \mathbf{v} and starting position \mathbf{a}_0 are chosen. A sequence of positions $\mathbf{a}_0, \mathbf{a}_1, \mathbf{a}_2, \dots$ is generated by $\mathbf{a}_{i+1} = \mathbf{a}_i + \mathbf{v}$. Whenever any of

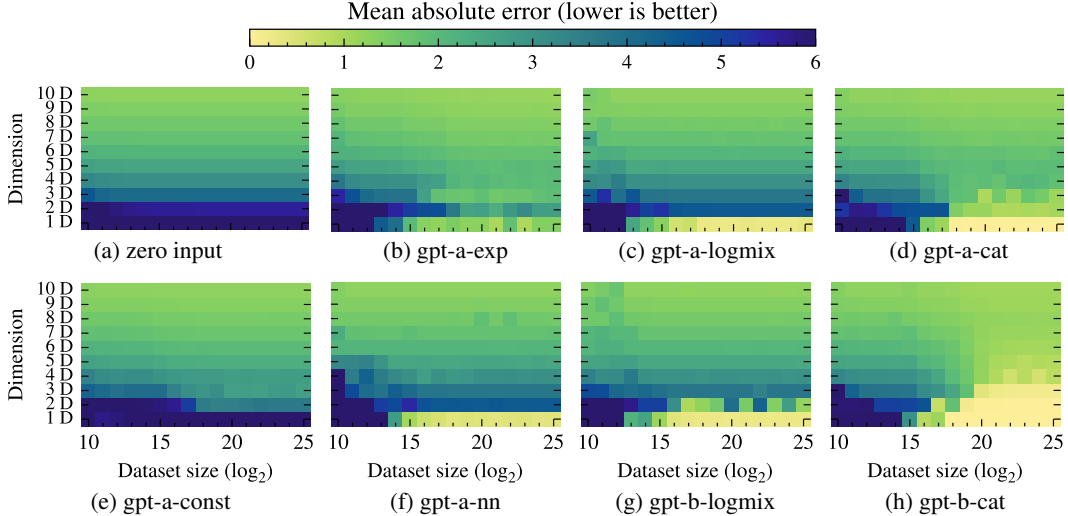


Figure 10: Performance comparison of 8 models in terms of test set mean absolute error (MAE). Each model is trained and evaluated over a landscape of 16 training set sizes for 10 modulo datasets. Model (a) takes no input and just outputs the empirical training set distribution; it acts as a baseline.

the components of \mathbf{a}_i overflow with respect to \mathbf{n} when transitioning to \mathbf{a}_{i+1} , an event is generated at time $t = i + 1$.

The 1D dataset is formed of many separate event sequences of length 1024 generated for different a_0 and v . To create a sequence, we sample a_0 uniformly from $[0, 1021)$ and v uniformly from $[10, 80]$ and generate 1024 events per sequence. The other 9 datasets are generated in the same way. Having many short sequences rather than a single long sequence makes the dataset more representative of datasets like the NYC taxi dataset, the Stack Overflow dataset and the chicken RGC dataset, all of which contain numerous separate sequences. More details on the generation process, including motivations for the bounds of v and an analogous continuous process, are described in Appendix C.4. For each dataset, we generate 2^{17} sequences, for a total of 2^{27} events per dataset. This is then split into training, validation and test sets in an 8:1:1 ratio. As before, we will consider 16 subsets of the training set, containing $2^0, 2^1, \dots, 2^{15}$ sequences ($2^{10}, 2^{11}, \dots, 2^{25}$ events).

6.2 Results and discussion

All 7 `gpt-a` and `gpt-b` based models from the previous section are trained on the modulo datasets. Figure 10 shows MAE for the models across the landscape of modulo datasets. NLL scores appear in Appendix A. The first figure, Figure 10a, is the result of using only the training set’s empirical distribution for prediction (no event history input is used) and acts as a baseline for comparison.

The first observation is that for all dimensions, there is a training set size above which `gpt-a-cat` is equal to or better than the other `gpt-a` models. This result is another example demonstrating the competitiveness of the categorical head when there is sufficient data. We also see the benefit of using larger models when training set sizes are large, demonstrated by a reduction in MAE for `logmix` and categorical heads when switching from `gpt-a` to `gpt-b`. There are also differences between models when using small training sets; for example, the `logmix` head is more effective than the categorical head. This effect is relatively insensitive to model size, which is evidence that the output structures themselves affect generalization when data is limited.

By comparing to the zero input baseline, we see that the information usable by each model decreases with increasing dimension—by 10D, even with 2^{25} samples, no model markedly outperforms the zero input baseline. From this perspective, the modulo datasets form a spectrum between easy (1D) and very difficult (10D) in terms of extracting information about the underlying event generating process. In the previous section, we hypothesized that the Poisson dataset was very difficult in this regard, whereas the Metropolis lognormal dataset allowed models to improve with more data. Figure 11 gives evidence for this interpretation by comparing the similarity between the two datasets against all

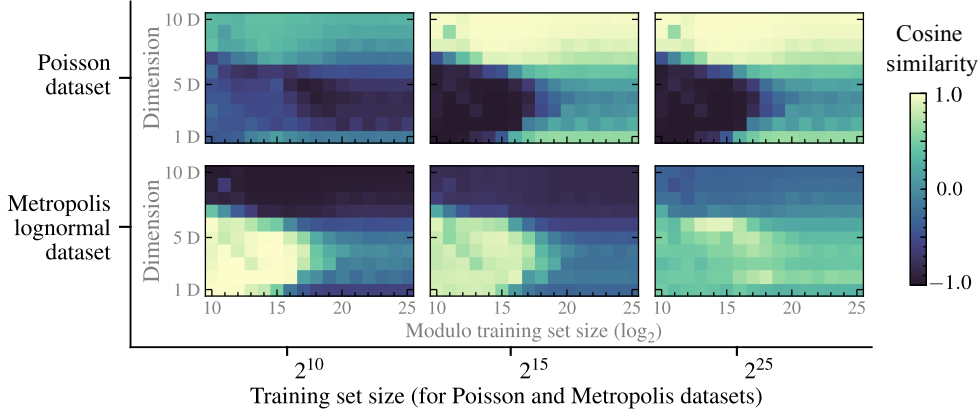


Figure 11: Dataset similarity between the Poisson dataset (**top**) at 3 training set sizes and the 160 modulo datasets, calculated as cosine similarity between vectors of NLL scores for models that were trained on both datasets. The same is shown (**bottom**) for the Metropolis lognormal dataset. The calculation is covered in more detail in Appendix C.4.

modulo datasets—the Metropolis dataset is more similar to the lower dimensional datasets compared to the Poisson dataset, which is more similar to the higher.

7 Discussion

A major argument of this work is that a task and dataset should drive model choice. In the spike prediction task, the task itself characterized a simple discrete output structure. Other datasets where there is a notion of discrete samples, such as the NYC taxi dataset, are also likely to benefit from a discrete distribution. When datasets are small, highly expressive outputs can generalize poorly in comparison to smaller models or those with constrained output structures. This suggests that both model size and output structure can be considered to have regularizing effects that can account for dataset dependent performance differences between models. For applications where there is abundant training data providing usable information about the underlying event generating process, we hypothesize that successful models will tend toward being larger and having more expressive/less constrained output structures. For the task of predicting neuronal spikes from multi-electrode arrays or embedded electrodes, our results suggest that the amount and properties of the data available will make a simple categorical output an effective choice.

8 Limitations

A number of limitations of the work reduce the strength of the conclusions. The work does not consider the prediction of additional spatial or categorical information. A compromise was made in terms of which models were trained. We aimed to test existing models in their original form. For RNN models, transitioning to the larger gpt-a meant an increase in parameter count *and* a significant change in architecture. This reduces the usefulness of parameter count as an explanatory variable. Similarly, the exposition of both discrete and continuous settings makes the treatment more comprehensive, but makes it more difficult to compare results across sections; for example, the NLL metric must switch from a density to mass interpretation. A benefit of the juxtaposition is that it highlights how NLL may not be an appropriate metric when datasets, such as the NYC taxi dataset, are inherently discrete; however, we do not explore this in detail. Another way this work provides only cursory treatment of a topic is how it broadly ascribes model capacity and output structure as being important for explaining generalization across datasets; however, specific mechanisms are not isolated such as data memorization or the alignment of the output distribution family to a dataset’s distribution. Discussion of concepts such as usable information is also broad and not expanded to be grounded in formulations such as those by Ethayarajh et al. [2022]. These limitations arose due to the work’s avoidance of a singularly focused treatment in favour of a heterogeneous treatment that highlights the benefits of expanding the scope of analysis in the field of neural TPPs.

9 Conclusion

The task of next spike prediction can be effectively performed using a simple transformer model with an unconstrained discrete probability mass output. This categorical output structure is also competitive on common TPP datasets when not in a data limited regime. Extending existing TPP datasets reveals that, for many of the datasets, the additional data provides little information usable by the models being trained. This explains the success of relatively small models on these datasets. We introduced a new synthetic dataset, the Metropolis lognormal dataset, where more data does afford models to learn more about the underlying event generating process. We introduce a family of synthetic datasets which allows the relationship between usable information and model performance to be explored in more detail. This investigation highlights the conditions (sufficient usable information) where using a larger model and a flexible output structure such as a categorical distribution is advantageous.

Acknowledgements

KD would like to acknowledge scholarship support from the Leverhulme Trust (DS-2020-065). TB acknowledges funding from the Wellcome Trust (Investigator Award in Science 220277/Z20/Z), the European Research Council (ERC-StG “NeuroVisEco” 677687 and ERC-AdG “Cones4Action” covered under the UK’s EPSRC guarantee scheme EP/Z533981/1), UKRI (BBSRC, BB/R014817/1, BB/W013509/1), the Leverhulme Trust (PLP-2017-005, RPG-2021-026 and RPG-2-23-042) and the Lister Institute for Preventive Medicine. This research was funded in part by the Wellcome Trust [220277/Z20/Z]. For the purpose of open access, the author has applied a CC BY public copyright licence to any Author Accepted Manuscript version arising from this submission.

References

- Rishabh Agarwal, Max Schwarzer, Pablo Samuel Castro, Aaron C Courville, and Marc Bellemare. Deep Reinforcement Learning at the Edge of the Statistical Precipice. In *Advances in Neural Information Processing Systems*, volume 34, pages 29304–29320. Curran Associates, Inc., 2021.
- Tanguy Bosser and Souhaib Ben Taieb. On the Predictive Accuracy of Neural Temporal Point Process Models for Continuous-time Event Data. *Transactions on Machine Learning Research*, March 2023. ISSN 2835-8856.
- Kevin Doran, Marvin Seifert, Carola A. M. Yovanovich, and Tom Baden. Spike Distance Function as a Learning Objective for Spike Prediction. In *Proceedings of the 41st International Conference on Machine Learning*, pages 11474–11500. PMLR, July 2024.
- Nan Du, Hanjun Dai, Rakshit Trivedi, Utkarsh Upadhyay, Manuel Gomez-Rodriguez, and Le Song. Recurrent Marked Temporal Point Processes: Embedding Event History to Vector. In *Proceedings of the 22nd ACM SIGKDD International Conference on Knowledge Discovery and Data Mining, KDD ’16*, pages 1555–1564, New York, NY, USA, August 2016. Association for Computing Machinery. ISBN 978-1-4503-4232-2. doi: 10.1145/2939672.2939875.
- Kawin Ethayarajh, Yejin Choi, and Swabha Swayamdipta. Understanding dataset difficulty with \mathcal{V} -usable information. In *Proceedings of the 39th International Conference on Machine Learning*, pages 5988–6008. PMLR, June 2022.
- Alex R. Gogliettino, Sasidhar S. Madugula, Lauren E. Grosberg, Ramandeep S. Vilku, Jeff Brown, Huy Nguyen, Alexandra Kling, Paweł Hottowy, Władysław Dąbrowski, Alexander Sher, Alan M. Litke, and E. J. Chichilnisky. High-Fidelity Reproduction of Visual Signals by Electrical Stimulation in the Central Primate Retina. *The Journal of Neuroscience: The Official Journal of the Society for Neuroscience*, 43(25):4625–4641, June 2023. ISSN 1529-2401. doi: 10.1523/JNEUROSCI.1091-22.2023.
- Kaiming He, Xiangyu Zhang, Shaoqing Ren, and Jian Sun. Deep Residual Learning for Image Recognition. In *2016 IEEE Conference on Computer Vision and Pattern Recognition (CVPR)*, pages 770–778, Las Vegas, NV, USA, June 2016. IEEE. ISBN 978-1-4673-8851-1. doi: 10.1109/CVPR.2016.90.

- Jeremy Howard, Sylvain Gugger, and Soumith Chintala. *Deep Learning for Coders with Fastai and PyTorch: AI Applications without a PhD*. O’Reilly Media, Inc, Sebastopol, California, first edition edition, 2020. ISBN 978-1-4920-4552-6.
- Jie Hu, Li Shen, and Gang Sun. Squeeze-and-Excitation Networks. In *Proceedings of the IEEE Conference on Computer Vision and Pattern Recognition*, pages 7132–7141, 2018.
- Hengguan Huang, Hao Wang, and Brian Mak. Recurrent Poisson Process Unit for Speech Recognition. *Proceedings of the AAAI Conference on Artificial Intelligence*, 33(01):6538–6545, July 2019. ISSN 2374-3468. doi: 10.1609/aaai.v33i01.33016538.
- Rob J. Hyndman and Yanan Fan. Sample Quantiles in Statistical Packages. *The American Statistician*, 50(4):361–365, 1996. ISSN 0003-1305. doi: 10.2307/2684934.
- Håvard Kvamme and Ørnulf Borgan. Continuous and discrete-time survival prediction with neural networks. *Lifetime Data Analysis*, 27(4):710–736, October 2021. ISSN 1572-9249. doi: 10.1007/s10985-021-09532-6.
- Shuang Li, Shuai Xiao, Shixiang Zhu, Nan Du, Yao Xie, and Le Song. Learning Temporal Point Processes via Reinforcement Learning. In *Advances in Neural Information Processing Systems*, volume 31. Curran Associates, Inc., 2018.
- Haitao Lin, Cheng Tan, Lirong Wu, Zicheng Liu, Zhangyang Gao, and Stan Z. Li. An Extensive Survey With Empirical Studies on Deep Temporal Point Process. *IEEE Transactions on Knowledge and Data Engineering*, 37(4):1599–1619, April 2025. ISSN 1558-2191. doi: 10.1109/TKDE.2024.3522114.
- Ilya Loshchilov and Frank Hutter. Decoupled Weight Decay Regularization, January 2019.
- Takahiro Omi, naonori ueda, and Kazuyuki Aihara. Fully Neural Network based Model for General Temporal Point Processes. In *Advances in Neural Information Processing Systems*, volume 32. Curran Associates, Inc., 2019.
- Stack Overflow. Stack Exchange Data Dump. <https://stackoverflow.com/help/data-dumps>, August 2024.
- Antonio R. C. Paiva, Il Memming Park, and Jose C. Principe. A comparison of binless spike train measures. *Neural Computing and Applications*, 19(3):405–419, April 2010. doi: 10.1007/s00521-009-0307-6.
- Alec Radford, Jeffrey Wu, Rewon Child, David Luan, Dario Amodei, and Ilya Sutskever. Language Models are Unsupervised Multitask Learners. *Technical report, OpenAI*, February 2019.
- Susanne Schreiber, Susanne Schreiber, Jean Marc Fellous, Diane Whitmer, Paul H. E. Tiesinga, and Terrence J. Sejnowski. A new correlation-based measure of spike timing reliability. *Neurocomputing*, 52:925–931, June 2003. doi: 10.1016/s0925-2312(02)00838-x.
- Marvin Seifert, Paul A. Roberts, George Kafetzis, Daniel Osorio, and Tom Baden. Birds multiplex spectral and temporal visual information via retinal On- and Off-channels. *Nature Communications*, 14(1):5308, August 2023. ISSN 2041-1723. doi: 10.1038/s41467-023-41032-z.
- Oleksandr Shchur, Marin Biloš, and Stephan Günnemann. Intensity-Free Learning of Temporal Point Processes, January 2020.
- Oleksandr Shchur, Ali Caner Türkmen, Tim Januschowski, and Stephan Günnemann. Neural Temporal Point Processes: A Review. In *Proceedings of the Thirtieth International Joint Conference on Artificial Intelligence*, pages 4585–4593, Montreal, Canada, August 2021. International Joint Conferences on Artificial Intelligence Organization. ISBN 978-0-9992411-9-6. doi: 10.24963/ijcai.2021/623.
- Leslie N. Smith. Cyclical Learning Rates for Training Neural Networks. *2017 IEEE Winter Conference on Applications of Computer Vision (WACV)*, pages 464–472, March 2017. doi: 10.1109/WACV.2017.58.

- Leslie N. Smith and Nicholay Topin. Super-Convergence: Very Fast Training of Neural Networks Using Large Learning Rates. <https://arxiv.org/abs/1708.07120v3>, August 2017.
- M. C. W. Van Rossum. A Novel Spike Distance. *Neural Computation*, 13(4):751–763, April 2001. doi: 10.1162/089976601300014321.
- Chris Whong. NYC’s Taxi Trip Data. https://chriswhong.com/open-data/foil_nyc_taxi/, March 2014.
- Yilun Xu, Shengjia Zhao, Jiaming Song, Russell Stewart, and Stefano Ermon. A THEORY OF USABLE INFORMATION UNDER COMPUTATIONAL CONSTRAINTS. 2020.
- Siqiao Xue, Xiaoming Shi, Zhixuan Chu, Yan Wang, Hongyan Hao, Fan Zhou, Caigao Jiang, Chen Pan, James Y. Zhang, Qingsong Wen, Jun Zhou, and Hongyuan Mei. EasyTPP: Towards Open Benchmarking Temporal Point Processes. <https://arxiv.org/abs/2307.08097v3>, July 2023.
- Simiao Zuo, Haoming Jiang, Zichong Li, Tuo Zhao, and Hongyuan Zha. Transformer Hawkes Process. In *Proceedings of the 37th International Conference on Machine Learning*, pages 11692–11702. PMLR, November 2020.

A Supplementary results

This appendix presents results supplementary to Sections 3 to 6.

Table 1 from Section 3 (*Mixed results on synthetic datasets from [Omi et al., 2019]*) showed results for rnn-logmix, gpt-a-logmix and gpt-a-cat evaluated on the 7 synthetic datasets from Omi et al. [2019]. These results are extended by Table 3 to include information on the variability over the 10 runs.

In Section 4 (*Training set sizes differentiate TPP model performance*), Figure 4 showed NLL scores on a subset of the synthetic datasets used in this work; Figure 12 below shows the complete set of NLL scores, including those for the Metropolis lognormal dataset from Section 5. The following figure, Figure 13, shows the MAE scores for the same models and datasets.

In Section 6 (*Event sequences from modulo addition*), results were reported in terms of MAE. The corresponding NLL scores are shown in Figure 14.

Table 3: Extension of Table 1 from Section 3 (*Mixed results on synthetic datasets from [Omi et al., 2019]*). Three models were evaluated in terms of test set NLL (lower is better) on 7 datasets generated following Omi et al. [2019]. Point estimates are the mean over 10 trials (training with 10 datasets generated with different random number generator seeds). Variability is expressed as 95% confidence intervals calculated assuming a normal distribution of the mean: $\pm 1.96 \frac{s}{\sqrt{10}}$, where s is the sample standard deviation.

Dataset	rnn-logmix	gpt-a-logmix	gpt-a-cat
Poisson	1.000 \pm 4.57e-05	1.000 \pm 4.56e-05	1.004 \pm 8.18e-05
Nonstationary Poisson	0.722 \pm 2.27e-04	0.696 \pm 1.36e-04	0.710 \pm 9.82e-04
Self-correcting	0.804 \pm 1.91e-04	0.763 \pm 1.95e-04	0.772 \pm 4.58e-04
Renewal	0.248 \pm 3.18e-05	0.248 \pm 7.30e-05	0.254 \pm 1.82e-04
Nonstationary renewal	0.379 \pm 3.59e-04	0.346 \pm 2.64e-04	0.361 \pm 7.58e-04
Hawkes1	0.448 \pm 3.91e-04	0.452 \pm 4.13e-04	0.467 \pm 6.49e-04
Hawkes2	-0.010 \pm 3.11e-04	-0.005 \pm 7.22e-04	0.018 \pm 7.55e-04

A.1 Discussion

The supplementary results motivate the discussion of two points: the contrast between MAE and NLL metrics, and the presence of infinite NLL scores.

The MAE scores on the synthetic and “real-world” datasets (Figure 13) show a similar pattern to the NLL scores (Figure 12). The greatest difference between the two metrics is seen on the NYC taxi dataset, where the categorical models’ precision at fine time scales does not translate to a markedly lower MAE score. This is further evidence to support the claim that NLL should be evaluated in terms of probability mass by specifying an interval of interest, such as hours, rather than evaluating in terms of probability density. Indeed, the best scoring model in terms of NLL evaluated as a density is a model that outputs arbitrarily larger probability densities to the countable rationals, yet such a model would not necessarily score well in terms of other metrics such as MAE.

Another observation from the comparison between MAE and NLL is that thp-0 and thp-1 score far lower in terms of MAE compared to NLL. These models have two output heads, one for specifying a probability distribution, and another for making point predictions, and the models are trained with a sum of negative log-likelihood and mean-squared error (MSE) loss terms using these heads [Zuo et al., 2020]. One possible explanation for the poor MAE scores is that, according to statistical decision theory, the median of a distribution minimizes the expected cost under an MAE cost model, whereas the mean of a distribution minimizes the expected cost under an MSE cost model. That is to say, it is possible that the MSE loss term is suboptimal for the task of point predictions evaluated in terms of MAE.

Infinite negative log-likelihood (zero likelihood) scores on the modulo datasets raise questions of numerical precision, overfitting and test set lengths. The NLL scores for the cyclic datasets (Figure 14) contain zero likelihood scores: the logmix head concentrates sufficiently little probability mass to the

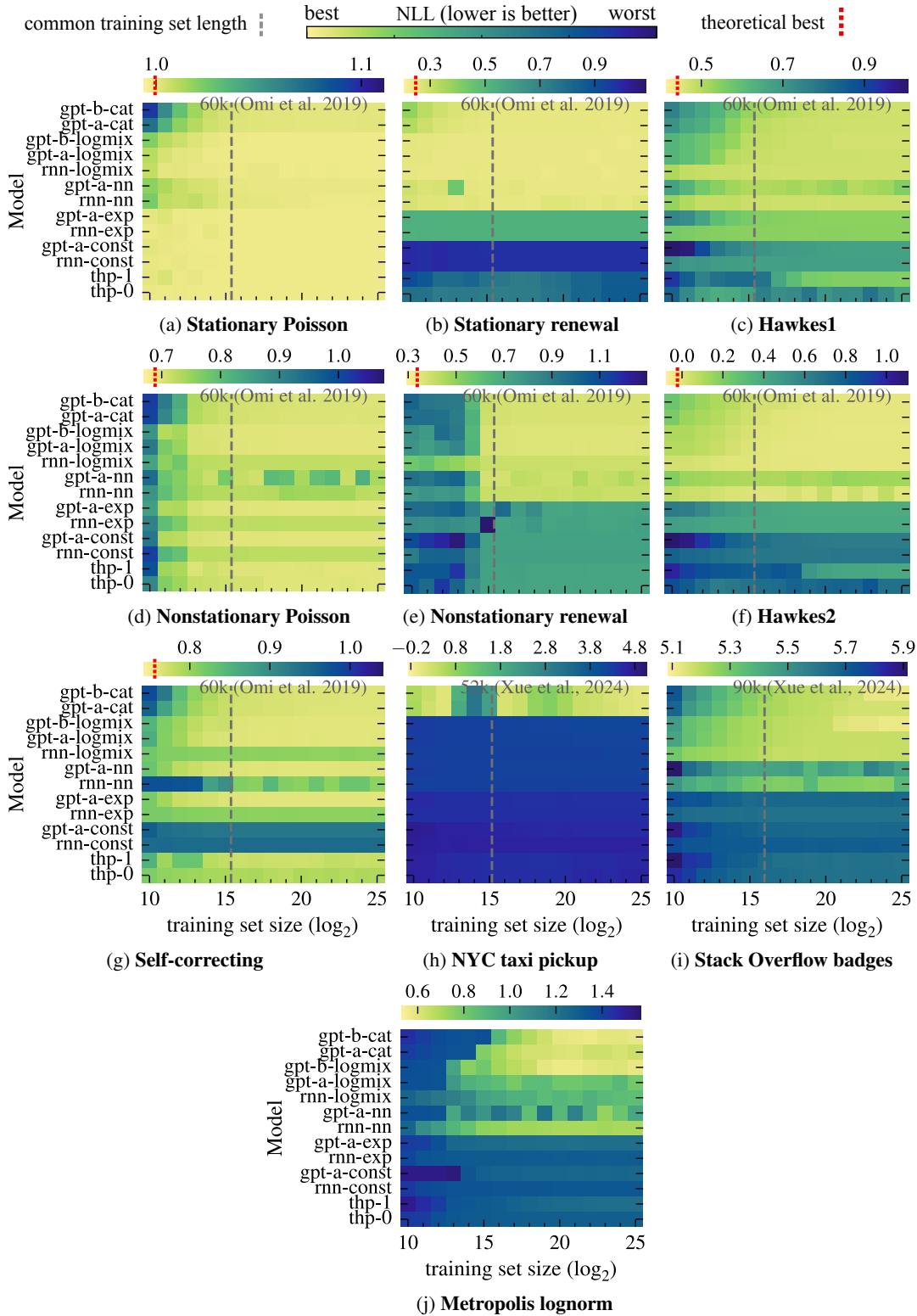


Figure 12: Performance comparison of 13 models in terms of test set NLL across 8 synthetic and two “real-world” datasets. There are 16 training set lengths from 2^{10} to 2^{25} . The colormap ranges span each sub-figure’s full range of values. For synthetic datasets where a theoretical best score is known, it is marked with a red dashed line.

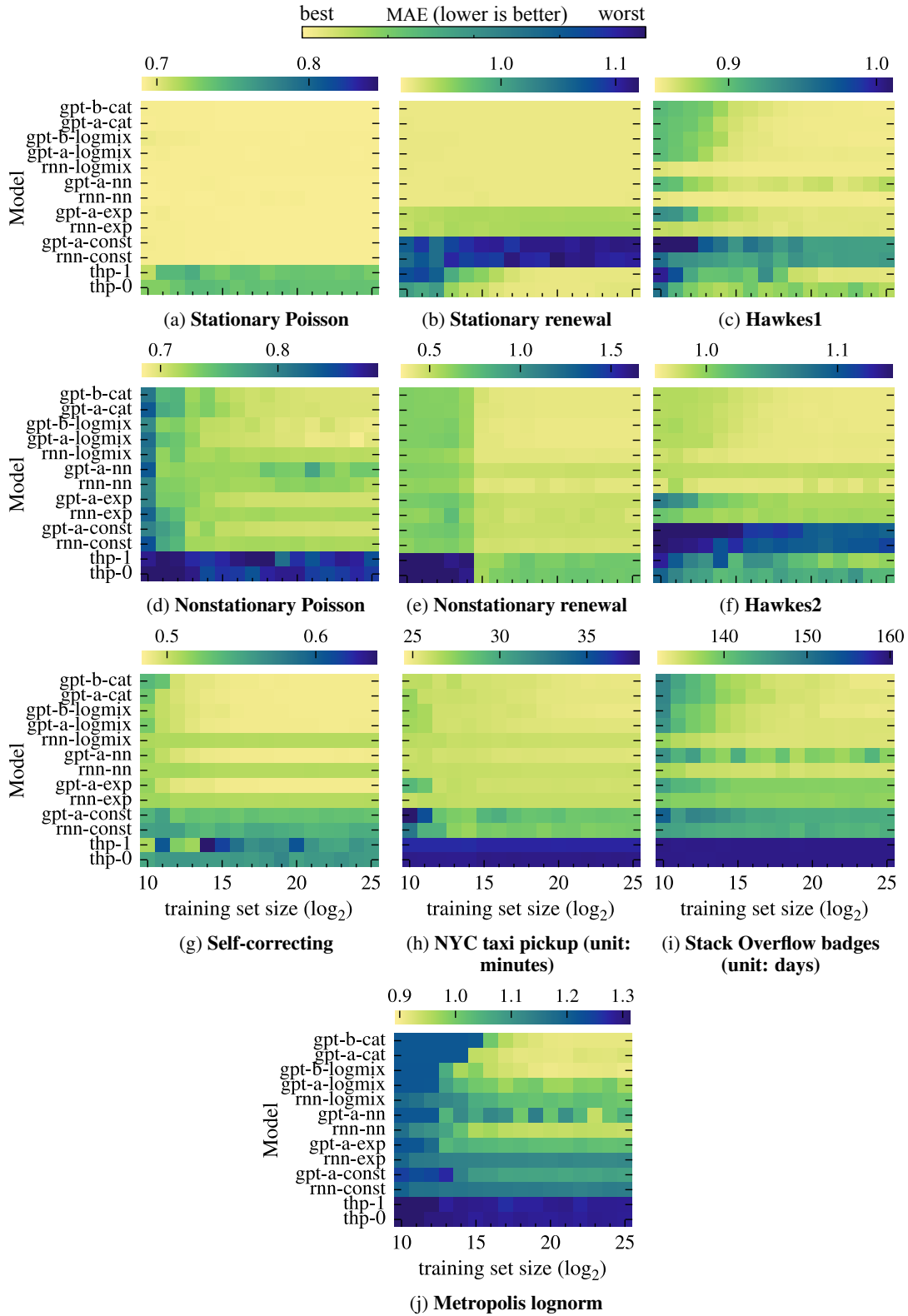


Figure 13: Performance comparison of 13 models in terms of test set MAE across 8 synthetic and two “real-world” datasets. There are 16 training set lengths from 2^{10} to 2^{25} . The colormap ranges span each sub-figure’s full range of values. The inter-event times for the NYC taxi dataset are scaled to minutes, and the Stack Overflow badges dataset is scaled to days.

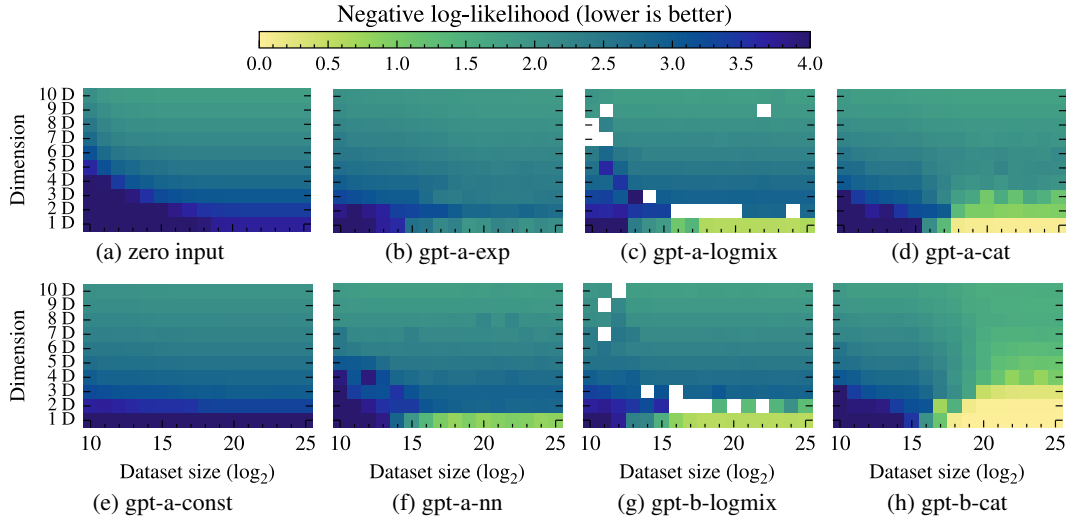


Figure 14: Performance comparison of 8 models in terms of test set NLL. Each model is trained and evaluated over a landscape of 16 training set sizes for 10 modulo datasets. Model (a) takes no input and just outputs the empirical training set distribution; it acts as a baseline. Likelihood is probability mass based and involves integrating over a 1-unit interval for models that output a continuous distribution. White (\square) represents a likelihood of 0 (∞ negative log-likelihood) and includes the case where a model assigns a likelihood low enough to encounter numerical issues.

interval containing the ground truth event that calculating the log probability produces the floating-point representation of negative infinity (when using `float32` precision). Although this occurs rarely, the relatively large test sets used in this work magnify the chance that this leads to an infinite NLL score. In part, this is a reflection of the issues of NLL as a metric; when viewing the performance of the logmix head in terms of MAE (Figure 10), there is no indication of this issue. A poor way to address this issue is to clamp the output probabilities above a minimum value—this causes the output distribution to no longer be a valid probability distribution by having infinite probability mass on the interval $[0, \infty)$. If the cause is a result of `gpt-a-logmix` or `gpt-b-logmix` being overconfident in certain values, a suitable solution could be to design a loss term that encourages at least one of the mixture components to have a relatively large variance (and non-zero mixture weight).

Table 4: Convolution layers of the stimulus and spike history encoder used for spike prediction. The model has ~ 2.00 M trainable parameters.

Layer	Input size	Kernels (length, channels, stride)	Output size
Conv 1	5×1024	$[21, 16, 2] \times 1$	16×512
Conv 2	16×512	$[21, 16, 1] \times 1$	16×512
ResNet block $\times 3$ (downsampling)	16×512	$\begin{bmatrix} 1 & 256 & 1 \\ 7 & 256 & 2 \\ 1 & 64 & 1 \end{bmatrix} \times 6$	64×64
ResNet block	64×64	$\begin{bmatrix} 1, & 256, & 1 \\ 7, & 256, & 1 \\ 1, & 64, & 1 \end{bmatrix} \times 4$	64×64

B Spike prediction

This appendix is supplementary to Section 2: *A categorical output is effective for spike prediction.*

B.1 Dataset

For the spike prediction task, we use the dataset constructed by Doran et al. [2024] from a multi-electrode array recording of chicken RGCs carried out by Seifert et al. [2023]. The dataset consists of 15 minutes of stimulus and spike activity for 60 RGCs at a sample rate of 992 Hz. The sample period is very close to 1 ms (1.0081), and when discussing model inputs and outputs we make the simplification of assuming 1 bin is 1 ms. This means that while the 80×1.0081 ms intervals actually sum to 80.65 ms, we refer to the combined 80 bin interval as being 80 ms for simplicity. An input to a model is a 5×1024 -shaped array representing just over 1 second of stimulus and spike history—4 rows record the 4-LED stimulus, and the last row records the spike train. For any given input, the ground-truth output is 1 of 81 possible events corresponding to a spike occurring in one of 81 intervals: 80 approximately 1 ms length intervals and the final infinite interval. The recording is broken into intervals along the time axis in order to form training, validation and test segments with a ratio (7, 2, 1). From a training, validation or test interval, a sample is formed from any sub-interval long enough to cover both input and output lengths (1024 + 80 bins).

B.2 Model architecture

The overall model architecture can be summarized as: `head(gpt(cnn(input) + embed(cell_id)))`, where the head is either the `logmix` or `discrete` head. The CNN and transformer architectures are described below. The embedding is a standard 1-hot vector encoding of the integer cell ID $\in [0, 60)$.

B.3 CNN encoder

The CNN encoder shared by all spike prediction models takes a 5×1024 -shaped input and produces a 64×64 shaped intermediate representation which is added to the cell ID embedding to form the input to the `gpt-a` or `gpt-b` transformers. The CNN architecture is described in Table 4. ResNet blocks [He et al., 2016] with an expansion factor of 4 form the core of the encoder. Squeeze and excite layers [Hu et al., 2018] were applied to the residual connections between ResNet blocks.

B.4 gpt-a and gpt-b

The gpt-a and gpt-b transformers follow the standard GPT-2 architecture ([Radford et al., 2019]) with the layer configurations (layers-heads-embedding size) set to 2-4-16 and 6-4-32 respectively. This gives gpt-a and gpt-b 108k and 1.20M trainable parameters, respectively. The standard GPT-2 small configuration defined by Radford et al. [2019] uses a 12-12-768 configuration, highlighting that both gpt-a and gpt-b are very small in the context of GPTs used as large language models. Computational limits prevented the investigation of larger models.

B.5 Output heads

For the spike prediction task, the two output heads were implemented as linear functions (fully-connected layers) taking the last vector of the transformer output as input. The logmix outputs $16 \times 3 = 48$ values used to parameterize a mixture of 16 log-normal distributions. The cat head outputs 81 values, used to parameterize the discrete distribution over 81 intervals.

B.6 Training

A batch size of 64 was used for all models. Models were trained over 2 epochs, which was empirically determined to be long enough to see all models eventually exhibit overfitting. While 2 epochs may seem low, the $10\frac{1}{2}$ minutes of the training set produces over 37 million unique timesteps ($10\frac{1}{2}$ minutes with 992 samples per second for 60 cells), and each of these appears as a model input 1024 times (the model input length) per epoch. Cross-entropy loss is used for both output heads. This is a probability density calculation for the logmix head, and a probability mass calculation for the cat head.

While training, evaluations were carried out at regular training step intervals—every 5000 training steps. With 37 million training samples and a batch size of 64, this corresponds to ~ 116 evaluations over the course of training.

Other training settings shared by other experiments are described in Appendix E.

B.7 Evaluation

Four metrics are used to describe the performance of models at the spike prediction task: negative log-likelihood, Van Rossum distance, Schreiber similarity and smoothed Pearson correlation. The metrics are calculated on a held-out test interval of the RGC recording.

B.8 Negative log-likelihood

Negative log-likelihood (NLL) is the mean negative log-likelihood of the ground truth spikes given a model’s output, calculated for every input-output snippet in the test set. This is a non-autoregressive metric. It is calculated in terms of probability mass, which involves integrating over the interval for the logmix head.

B.8.1 Spike train similarity/difference metrics

The remaining 3 metrics are calculated after first producing a predicted spike train. A spike train is produced by evaluating a model autoregressively, shifting forward until the time of the next predicted spike or the maximum stride of 80 bins. A model is given the first input snippet including the ground truth spikes. The median of the model’s output distribution is used as the prediction for the next spike. For example, if there is a spike predicted in the 10th bin, then nine 0s and one 1 will be appended to the existing spike train. This process repeats until the stimulus is fully consumed.

Once a spike train is generated, Van Rossum distance, Schreiber similarity and smoothed Pearson correlation can be calculated. The process of calculating Van Rossum distance and Schreiber similarity is shown in Figure 15. Smoothed Pearson correlation is calculated as the well-known Pearson correlation after first smoothing with a Gaussian kernel. For all metrics, the smoothing parameter is set to 60 ms, which is a length shown to be appropriate by Doran et al. [2024].

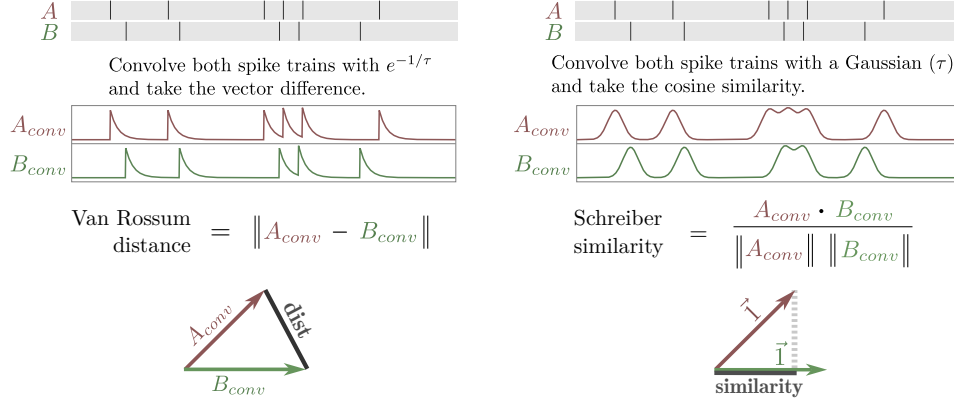


Figure 15: Calculation of Van Rossum distance (**left**) and Schreiber similarity (**right**) from two input spike trains. Both metrics employ distinct smoothing kernels to produce an intermediate vector. Van Rossum distance can be thought of as measuring the Euclidean distance between the vectors, while the Schreiber similarity assesses the angle between them. Figure taken from Doran et al. [2024].

B.9 Supplementary results

The main results of this work focus on probabilistic prediction. However, the spike train similarity/distance metrics do not require a probabilistic model, and it is interesting to extend the comparison to consider non-probabilistic models. Figure 16 shows the model comparison from Section 2 extended to include the spike distance head introduced by Doran et al. [2024]. On the non-probabilistic metrics, this output outperforms the two probabilistic approaches. This suggests that for contexts where application specific metrics are available, non-probabilistic models should also be considered.

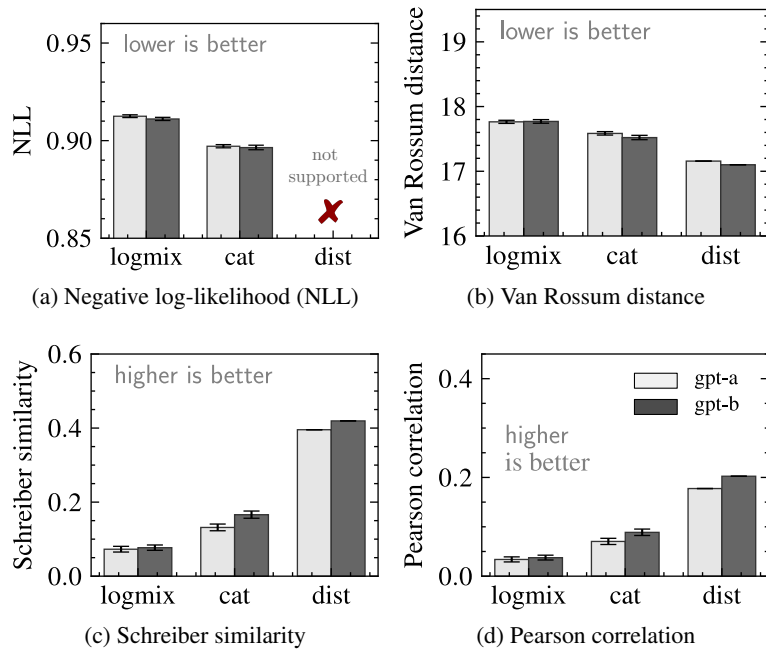


Figure 16: Performance comparison between three neural network outputs for spike prediction: *logmix* (a 16-component lognormal mixture distribution), *cat* (an 81-bin probability mass function) and *dist* (spike distance function—a non-probabilistic output introduced by Doran et al. [2024]). NLL is reported on the left, followed by three spike train similarity/distance metrics, evaluated autoregressively; they share a smoothing parameter of 60 ms. The shared base architecture is tested in two sizes: *gpt-a* and a larger *gpt-b*. Metrics are reported as interquartile means over the 60 chicken RGCs over 10 training repeats, with 95% bootstrap confidence intervals as error bars.

C Datasets

This appendix describes the datasets used in Sections 3 to 6. Appendix C.1 and Appendix C.2 explain the extension of existing datasets to accommodate larger training set lengths.

C.1 Synthetic datasets from [Omi et al., 2019]

We generate the 7 synthetic datasets from [Omi et al., 2019] following the released code that accompanied that work. We extended the length of the generated sequences to fill training, validation and test sets of size 2^{25} , 2^{17} and 2^{17} respectively. Where 10 training runs were carried out (Section 3), the training set was regenerated 10 times, each time using a different pseudo-random number generator seed. All datasets used the same validation and test sets from the first run.

C.2 NYC taxi pickup times and Stack Overflow badges

While there are many “real-world” datasets used in literature on TPPs, most are relatively small with less than 1 million events. New York City taxi pickup times and Stack Overflow badges were chosen for this work as the source data contains tens of millions of events, allowing a wide range of training set sizes to be investigated.

Data on taxi pickup times in various cities has been used in numerous works on TPPs. We use the data collected by Whong [2014]. This data is used in works such as [Du et al., 2016]. The data was obtained by Whong [2014] through filing a Freedom of Information Law Request (FOIL) to the New York City Taxi and Limousine Commission. The data comprises of millions of rows where each row contains (among other information): medallion ID, pickup datetime and dropoff datetime. For example: ["89D227B655E5C82AECF13C3F540D4C", "2013-01-01 15:11:48", "2013-01-01 15:18:10"]. The pickup and dropoff datetimes are recorded with a resolution of seconds. We process this data by grouping all entries by medallion, sorting by pick-up time to create a list of event sequences, and then subtracting adjacent event times to form sequences of inter-event times. Subsets of this list of lists are used to form the training, validation and test sets. The training set is formed by taking the first n sequences such that the n sequences contain at least 2^{25} inter-event times. The validation set is taken next followed by the test set such that each has at least 2^{17} inter-event times. The remaining events are not used. While data is recorded at a resolution of seconds, we rescale the data to units of minutes. We do no further processing of the data. This is in contrast to Du et al. [2016] who split sequences at gaps larger than 12 hours. We hypothesize that splitting at large gaps would benefit models which are less capable of expressing distributions with peaks far from zero; for example, a model outputting a constant hazard (equivalent to a parameterized Poisson distribution), cannot concentrate probability far from zero without also increasing the distribution’s second moment. We argue that there is no fundamental reason why models should not be expected to model these gaps, and so we do not split any sequences.

Timestamps of users receiving badges on the website Stack Overflow were also used by Du et al. [2016]. In order to complete training, validation and test sets of size 2^{25} , 2^{17} and 2^{17} , we obtained a more recent data export (last updated 29th August 2024) of the data from the Stack Overflow website [Overflow, 2024]. Timestamps for this dataset are recorded with a resolution of milliseconds. Processing was carried out in the same manner as for the NYC taxi dataset described above, this time grouping by the column `UserId`, and rescaling to units of days. At the time of download, Stack Overflow stipulated that the data was provided under the condition that the data is for the users’ own use; and so we do not distribute a copy.

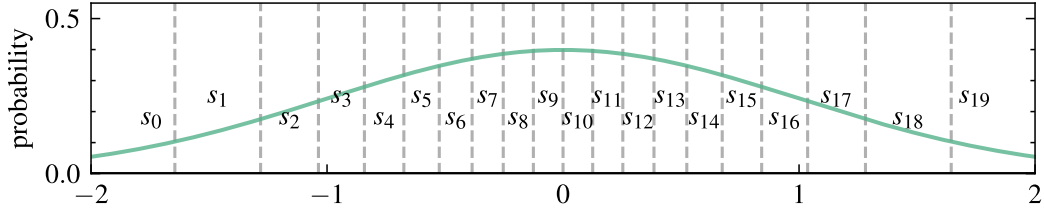


Figure 17: The interval $(-4.26, 4.26)$, which contains all but 2×10^5 of the probability mass of the standard normal distribution, is divided into 20 subintervals, each containing equal probability mass with respect to the standard normal. The outer intervals, $(-\infty, -4.26)$ and $(4.26, \infty)$, are not used. The intervals are labelled s_0, s_1, \dots, s_{19} corresponding to the states used in the Metropolis-Hastings sampler. Here, the figure zooms in to $(-2, 2)$ to see the shorter intervals more clearly.

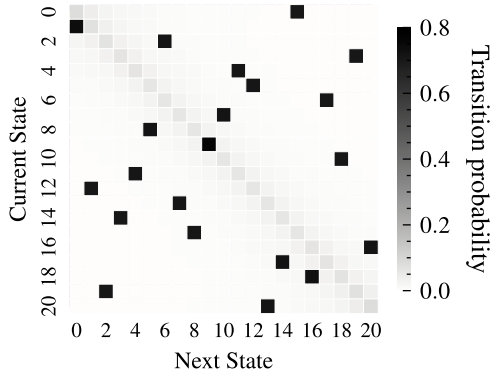


Figure 18: The stochastic state transition matrix used by the outermost sampler. The preponderance of probability is assigned to the next state of a random cycle, with a small amount of probability assigned down the diagonal. Reducing the probability assigned to the diagonal increases the determinism of the sampler, but reduces how well the sampler approximates the target distribution.

C.3 Metropolis lognormal process

Both the Metropolis lognormal event sequences and the modulo sequences were designed to be decodable to a high degree given sufficient event history and compute. They were also designed so that unconditional inter-event times follow a relatively simple distribution—this is intended to match real-world processes which can be fully deterministic given enough information yet have aggregate properties that follow simple distributions.

The Metropolis lognormal process achieves this by being generated from a poor sampler of a lognormal distribution. The inter-event times are approximate draws from a lognormal distribution, achieving one of the goals above, but the sampling is determined by a fixed transition matrix, which can be decoded given a sufficiently long sequence. The sampler is a modified Metropolis-Hastings algorithm, described in Algorithm 1. The sampler’s target distribution is a standard normal distribution, and the events of the process are obtained by taking the log of outputs of the sampler. A sampler uses a stochastic transition matrix like that shown in Figure 18. The proposed samples are generated with another modified Metropolis-Hastings sampler. In total, there is a stack of 3 such samplers, as described in Algorithm 1.

Algorithm 1 Modified Metropolis-Hastings sampler. A subset of the real line (t_{\min}, t_{\max}) is subdivided into S intervals of equal probability mass according to the target distribution π ; these S intervals are the states. Before querying the proposal distribution, the algorithm transitions according to a stochastic transition matrix between these states. To calculate the forward and reversal probability, an approximating distribution, `innerPdf`, is used. The sampler calls the step function in a loop, and, unlike standard Metropolis-Hastings, repeated samples are discarded. The samplers can be stacked; in this work, we stack 3 such samplers, and for the base distribution q_0 , a deterministic cycle between 30 quantile points of a normal distribution is used. This makes the sequence deterministic up to the randomness implied by the transition matrices, T_1, T_2 and T_3 and the uniform sampling, \mathcal{U} .

```

1: function mapPos( $x, s_{\text{from}}, s_{\text{to}}$ )
2:   Compute the relative position of  $x$  within the interval of state  $s_{\text{from}}$  and map it to the corresponding position in the interval of state  $s_{\text{to}}$ .
3:   return mapped position
4: function posToState( $x$ )
5:   Determine the state the given position  $x$  is in.
6:   return state
7: function Sampler.init( $x_0, \pi, T, \text{innerSampler}, \text{innerPdf}$ )
8:   The innerSampler is called to generate new proposals, and innerPdf is called to approximate the distribution of the innerSampler for the purpose of calculating the reversal probability.
9:   State:  $x_t \leftarrow x_0$ 
10:  State:  $\pi, q, T, \text{innerSampler}, \text{innerPdf}$ 
11: function Sampler.step
12:   $s_t \leftarrow \text{posToState}(x_t)$  ▷ Determine current state
13:   $s' \leftarrow \text{Sample from } T(s' | s_t)$  ▷ Transition to next state
14:   $x' \leftarrow \text{mapPos}(x_t, s_t, s')$ 
15:   $x_{t+1} \leftarrow \text{innerSampler}(x_{t+1} | x')$  ▷ Propose new sample
16:   $p_{\text{forward}} \leftarrow T(s' | s_t) \text{innerPdf}(x_{t+1} | x')$ 
17:   $p_{\text{reverse}} \leftarrow \sum_{i \in S} \text{innerPdf}(x_t | \text{mapPos}(x_{t+1}, s', s_i)) T(s' | s_i)$ 
18:  Compute acceptance ratio:
      
$$\alpha \leftarrow \frac{\pi(x_{t+1}) p_{\text{reverse}}}{\pi(x_t) p_{\text{forward}}}$$

19:   $u \leftarrow \text{Sample from } \mathcal{U}(0, 1)$ 
20:  if  $u < \alpha$  then
21:    return  $x_{t+1}$  ▷ Accept proposal
22:  else
23:    return  $x_t$  ▷ Reject, keep current state
24: function Sampler.sample
25:   $x_{t+1} \leftarrow \text{Sampler.step}$ 
26:  while  $x_{t+1} = x_t$  do ▷ Ignore repeated samples
27:     $x_{t+1} \leftarrow \text{Sampler.step}$ 
28:   $x_t \leftarrow x_{t+1}$  ▷ Update state
29:  return  $x_{t+1}$ 
30: function nestedSampler( $q_0$ )
31:   $\pi_1 \leftarrow \mathcal{N}(0, 1)$ 
32:   $\pi_2 \leftarrow \mathcal{N}(0, \frac{1}{3})$  ▷ Inner samplers are narrower
33:   $x_0 \leftarrow 0$ 
34:   $T_1, T_2, T_3 \leftarrow \text{sample transition matrices}$ 
35:   $q_1 \leftarrow \text{Sampler.init}(x_0, \pi_1, T_1, q_0, \pi_2)$ 
36:   $q_2 \leftarrow \text{Sampler.init}(x_0, \pi_2, T_2, q_1, \pi_2)$ 
37:   $q_3 \leftarrow \text{Sampler.init}(x_0, \pi_2, T_3, q_2, \pi_2)$ 
38:  return  $q_3$ 

```

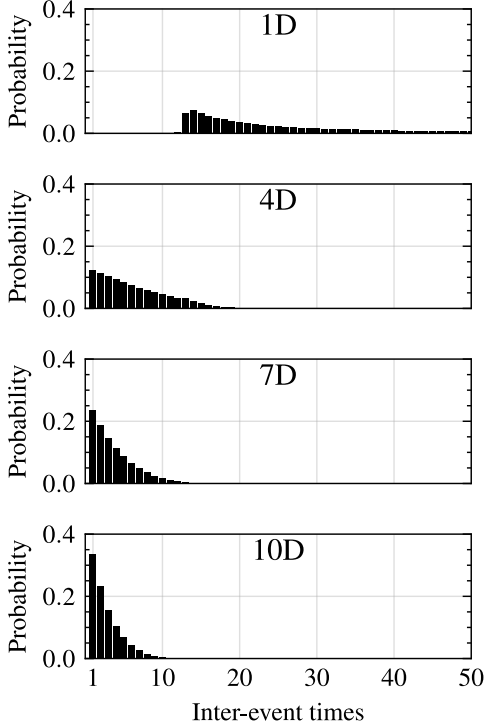


Figure 19: Training sets. Distribution of inter-event times for overflow datasets of dimension 1, 4, 7 and 10 (from top to bottom). The distribution is the count distribution of inter-event times over the 0.8×2^{17} sequences in the training set.

C.4 Modulo sequences

This section describes further details of the modulo “overflow” sequences. Appendix C.5 describes the properties of the inter-event time distributions of the modulo sequences. Appendix C.6 rephrases the sequences in terms of cyclic groups, which allows the easy deduction of the period of the sequences. Appendix C.7 describes analogous continuous time sequences. Appendix C.8 explains the motivation behind the bounds on the velocity v used to generate the sequences in this work.

C.5 Properties of the modulo datasets

This section builds some intuition on the modulo datasets. Figure 19 shows the distribution of inter-event times for the 1, 4, 7 and 10-dimension datasets. With increasing dimension, the distribution of inter-event times shifts to concentrate near 1, with a roughly exponential shape. The entropy of all 10 datasets is shown in Figure 20. The decreasing entropy with increasing dimension explains how the NLL scores for the zero input model (Figure 14a) decrease (improve) with increasing dimension. This is also demonstrated in Figure 21, where the cross-entropy between the full training set and smaller training sets predicts the NLL scores of the zero input model; the distributions of subsets with more than 2^9 sequences (2^{19} events) can be seen to be very similar to the overall distribution. Finally, Figure 22 uses \mathcal{V} -information [Xu et al., 2020] as applied by Ethayarajh et al. [2022] to gauge how difficult the datasets are for the gpt-b-cat model to learn beyond what the zero input model can learn. Interestingly, for some of the dimensions, there is a U-shaped relationship where at both small and large dataset sizes, the gpt-b-cat model can outperform the zero input model to a greater degree compared to intermediate dataset sizes.

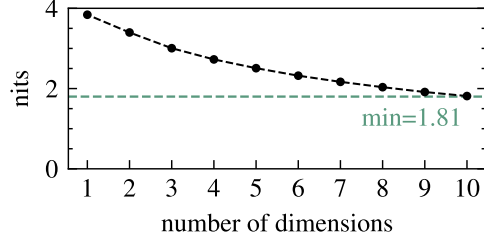


Figure 20: Entropy of the count distribution of inter-event times for each of the 10 training set.

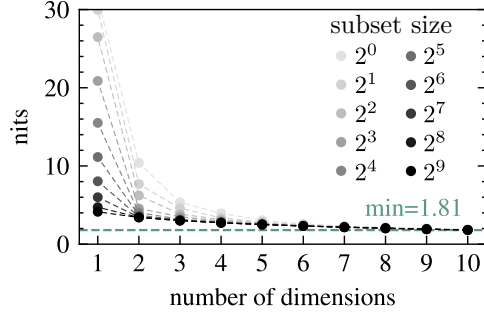


Figure 21: Mean cross-entropy between the distribution of inter-event times in the whole training set and in subsets of the training set. For 10 subset sizes ranging from 2^0 to 2^9 , the mean cross-entropy is calculated using 100 random subsets of that size. Subset sizes 2^9 and above are indistinguishable on the figure.

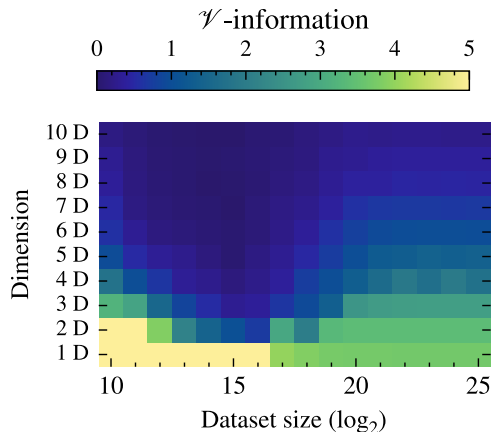


Figure 22: \mathcal{V} -information calculated following Ethayarajh et al. [2022] as $H_{\mathcal{V}}(Y) - H_{\mathcal{V}}(Y|X)$, where $H_{\mathcal{V}}(Y)$ is estimated from the cross-entropy from Figure 21 and the gpt-b-cat model results in Figure 14 are used for $H_{\mathcal{V}}(Y|X)$. The set \mathcal{V} is the set of all possible mappings describable by the gpt-b-cat architecture. Estimating $H_{\mathcal{V}}(Y)$ from the cross-entropy is possible as a gpt-b-cat model trained with no input will match the empirical distribution of the inter-event times in the provided training set.

C.6 Cyclic group perspective

The sequence $(\mathbf{a}_k)_{k=0}^{\infty}$ of particle positions in d dimensions can be understood as stepping through a sub-cycle of a cyclic group. In 1-dimension, for a given $n \in \mathbb{N}$, two elements c and g of the cyclic group $\mathbb{Z}/n\mathbb{Z}$ define the sequence $(a_k)_{k=0}^{\infty}$ as cg^k . The overflow sequence contains every k such that $cg^k < cg^{k-1}$. Moving to higher dimensions, let G be the product of d cyclic groups G_1, G_2, \dots, G_d of order n_1, n_2, \dots, n_d . Let c and g be elements of G and, as before, define the sequence $(g_k)_{k=0}^{\infty}$ as cg^k , with the overflows now defined as the k s where any element of cg^k is less than the previous element in cg^{k-1} . If all n_1, n_2, \dots, n_d are chosen to be prime, then it is guaranteed that all sequences will have a period of $n_1 \times n_2 \times \dots \times n_d$. As long as this product is less than the input length of a model, we can be confident that a model is not simply repeating a loop seen in its input.

C.7 Continuous sequences

A continuous analogue in 1-dimension is to consider a particle starting from position $p_0 \in \mathbb{R}$ and moving in a straight line with velocity $v \in \mathbb{R}$. An event occurs at every time $t > 0$ such that $p_0 + vt = kn$ for some $k \in \mathbb{N}$ and fixed $n \in \mathbb{R}$. An event sequence is then defined as the ordered set of all such t . This extends naturally to higher dimensions by considering vectors \mathbf{p}_0, \mathbf{v} and \mathbf{n} , and having events occur every time one of the components of $\mathbf{p}_0 + \mathbf{v}t$ is an integer multiple of the corresponding component of \mathbf{n} .

More complicated sequences can be generated by adding more particles or making them bounce rather than pass through faces, or making the task to determine the next collision time of a set of particles with mass moving in a box.

C.8 Bounds on v

An upper bound on v prevents the inter-event time distribution from collapsing to $\mathbb{P}(\Delta t = 1) = 1$ as the dimension increases. For example, in 10-dimensions, if components of \mathbf{v} are around 500, with the grid being defined by $\mathbf{n} = [1021]^d$, then each component overflows every 2-3 steps, resulting in almost every step containing an event. In this work, the upper bound on v was set to 80 to limit this effect.

The reason for the lower bound of 10 is that it sets the maximum inter-event time at around 100 (103). The benefit of this is that it allows the discrete approach to encode all possible event times with a reasonable array size. This marks a similarity to the spike prediction task, where 81 bins were sufficient to encode all events of interest. If there is a larger maximum inter-event time, then the

discrete model can use a larger output array or group events into a single output bin, similar to how bins were chosen in Section 3.

C.9 Cosine similarity

In Section 6 (*Event sequences from modulo addition*), Figure 11 shows the similarity of the Metropolis lognormal and Poisson datasets to the landscape of the modulo datasets. This section describes the calculation behind that figure.

For the top left subfigure (Poisson dataset at training set length 1024 compared to the modulo datasets) a value at position (i, j) of the grid is calculated as $\|\mathbf{a}\| \|\mathbf{b}_{ij}\| \cos \theta$, where \mathbf{a} is a length 7 vector that includes the normalized NLL scores on the Poisson dataset with training set length 1024 of the 7 models that appear in Figure 10. \mathbf{b}_{ij} is the length 7 vector of normalized NLL scores for the same models on the modulo dataset with dimension i and training set length indexed by j . Normalization of the NLL vectors can be done in various ways. We normalize the modulo dataset scores by the mean and standard deviation of all finite NLL scores across all modulo datasets and models. For the datasets being compared (for example the Poisson dataset at a certain training set length), the scores can be far more concentrated at a good score, and so the mean is not a good representation of the midpoint between good and bad scores. Instead, we use the theoretical best NLL score or best-recorded score (whichever is lowest) as a reference point for a good score and use the worst recorded score or the entropy of the inter-event time distribution (whichever is highest) to represent a bad score. These two extremes are interpreted as -1 and 1 respectively, and the NLL scores are normalized accordingly.

D Model details

This section covers some details on implementing the models used in this work. More details on how a categorical distribution can be mapped to a distribution over $[0, \infty)$ is covered in Appendix D.1. Encoding event times to be input to `gpt-a` and `gpt-b` is covered in Appendix D.2. Appendix D.3 describes the implementation of the existing models used in this work.

D.1 Bin widths for the discrete head with continuous data

When the target distribution is constrained to a small finite number of possibilities, as is the case for the spike prediction task and the modulo datasets, the discrete head can output an array of unnormalized probabilities with one element per possible event. This strategy does not work when the target distribution is closer to being continuous, as is the case for the datasets used in Sections 3 to 4. As described in Section 3, in this work, we follow Kvamme and Borgan [2021] and split the domain of the target distribution into intervals (as many intervals as we have output elements) that evenly share the probability mass of the training set’s empirical distribution. In this work, the domain is always assumed to be $[0, \infty)$, and the discrete models always output 128 elements. The endpoints of the intervals are determined as follows. The first interval begins at 0 and the last interval extends to ∞ . The 127 remaining boundaries are assigned to the $1/128, 2/128, \dots, 127/128$ quantiles of the inter-event times from the training set. The quantiles are calculated using the default `numpy` quantile function, which uses the linear interpolation method from [Hyndman and Fan, 1996]. Figure 23 shows an example output from a trained `gpt-a-cat` model with 128 output elements.

D.2 Input encoding for `gpt` based models

When the `gpt-a` and `gpt-b` architectures are used for the spike prediction task, the input to these modules is a sequence outputted by the CNN encoder. When the `gpt-a` and `gpt-b` architectures are used on their own in sections Section 3 onwards, the scalar values representing inter-event times are converted to a vector representation according to Algorithm 2 before being input into the transformers. This approach is similar to that used by Zuo et al. [2020]. We do not hard-code the sinusoidal frequencies but choose appropriate scales so that both long and short intervals seen in the data are captured.

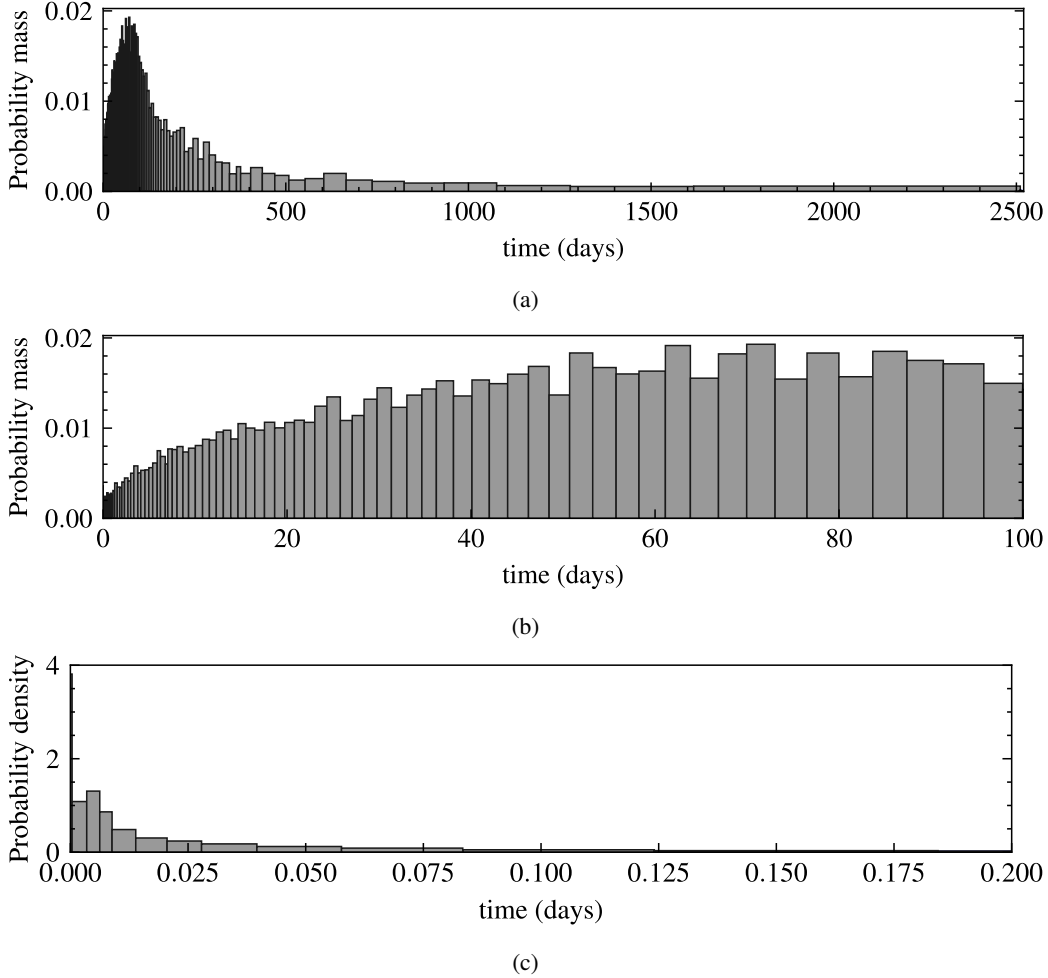


Figure 23: An example output of a gpt-a-cat model trained on the 2^{25} length Stack Overflow badges training set. **(a)**: the probability mass assigned to each of the 128 output intervals. The bar widths correspond to the interval widths and heights correspond to the probability mass assigned to the intervals by the model. The final infinite interval starts from 2511 and is assigned only a small probability (7.5×10^{-5}), so cannot be seen. **(b)**: the same output as (a), but zoomed in to the interval $(0, 100)$. **(c)**: zoomed into the interval $(0, 0.2)$, but this time, the bar heights correspond to the probability density over the intervals (mass/width). In this example, the probability density is highest for the very narrow intervals near 0.

Algorithm 2 Encode a scalar value v into a vector of even size n . v_{epsilon} should be chosen near the smallest inter-event time expected to be encountered and v_{max} should be chosen to be near the largest time expected to be spanned by inputs to the model, and will depend on the length of a model's input. In this work, we choose v_{epsilon} as the smallest inter-event time observed in the training set, and v_{max} as the largest time between events t_i and t_{i+L} where L is the input length of the model.

```

1: function encodeValue( $v, v_{\text{epsilon}}, v_{\text{max}}, n$ )
2:    $\text{scale}_{\text{min}} \leftarrow 2\pi/v_{\text{max}}$                                 ▷ Or use  $\frac{3}{2}\pi$  to add a little more range
3:    $\text{scale}_{\text{max}} \leftarrow 2\pi/v_{\text{epsilon}}$ 
4:    $\text{scale} \leftarrow \text{linspace}(\log(\text{scale}_{\text{min}}), \log(\text{scale}_{\text{max}}), n/2)$     ▷ A vector of length  $n/2$ 
5:    $x_1 \leftarrow \cos(\exp(\text{scale}) \cdot v)$ 
6:    $x_2 \leftarrow \sin(\exp(\text{scale}) \cdot v)$ 
7:    $x \leftarrow \text{concat}(x_1, x_2)$ 
8:   return  $x$ 

```

D.3 Existing models

The `rnn-const`, `rnn-exp` and `rnn-nn` models are implemented following the code accompanying [Omi et al., 2019]. The `rnn-logmix` model is implemented following the code accompanying Shchur et al. [2020]. The `thp-0` and `thp-1` models are implemented partially following [Zuo et al., 2020], but deferring to the implementation accompanying [Xue et al., 2023] for a number of bug fixes to the original model.

One deviation from these implementations is in model initialization. In order to improve convergence speed and stability while training, all models were initialized so that their outputs have first and second moments similar to those of the training set’s empirical distribution.

E Training and evaluation details

This appendix describes hyperparameters and other settings associated with training and evaluation. Appendix E.1 covers settings shared by all experiments. Settings specific to the spike prediction task were covered in Appendix B.6. Appendix E.2 covers settings associated with the remaining experiments.

E.1 Shared settings and hyperparameters

The following settings were shared across all training runs across all experiments.

Software. Pytorch 2.6.0 with Cuda 12.4.1 was used for training and evaluation.

Optimizer. All training runs use the AdamW optimizer described by [Loshchilov and Hutter, 2019]. AdamW parameters (β_1 , β_2 , eps, weight decay) were set to (0.9, 0.99, 1×10^{-5} , 0.02)—chosen roughly in line with heuristics described by Howard et al. [2020]. Weight decay was applied to all parameters except bias and embedding parameters.

Precision. Pytorch’s automatic mixed precision and gradient scaling were used during training. In cases where greater numerical precision is needed, such as when calculating probabilities from hazard outputs, 32-bit floating-point precision was used.

Loss function. Most models were trained to minimize negative log-likelihood. The spike distance model that appears in Appendix B was trained to minimize the mean-squared error between the output and target representations. `thp-0` and `thp-1` used a loss term that is the sum of a negative log-likelihood term and a mean-squared error term [Zuo et al., 2020].

Model choice. The final models are selected from the checkpoints taken during training with the lowest validation loss.

Learning rate scheduler. The 1-cycle learning rate policy with 3 phases described by Smith and Topin [2017] was used.

Maximum learning rate. The maximum learning rate, which parameterizes the learning rate scheduler, was chosen by carrying out learning rate range tests as described by Smith [2017]. The choice of learning rate is described in more detail below, in Appendix E.3.

Early stopping. An early-stopping strategy was used to reduce wasted compute. After at least 1/2 of the total training steps have been completed (when the learning rate is decreasing), early stopping is triggered if the smoothed validation loss (smoothed at 0.8) has not improved over 12 evaluations. Post-training, training and validation loss curves were inspected to ensure that early stopping was not triggered prematurely.

E.2 Settings for experiments from Sections 3 to 6

The approach to hyperparameter selection described in this section is used for the experiments from Section 3 onwards. The choice of settings such as batch size, training duration and learning rate is more involved for these experiments, as the heterogeneous combinations of models and datasets require a more sophisticated choice of hyperparameters.

Training steps. In order to compare training runs across datasets of different sizes, the number of epochs is not fixed. We set two upper limits: the number of samples drawn during training is capped

at 2^{27} (~134 million samples), and the number of epochs is capped at 512. These limits are large enough so that both the larger and smaller datasets are trained for sufficient samples in order for training to converge (or overfit). The longest training set has 2^{25} events, and so each sample can be seen 4 times during training. For training sets sizes smaller than 2^{19} , samples will be seen 512 times during training. The combination of these caps with the batch size settings described next results in the training settings shown in Table 5.

Batch size. The wide range of training set sizes means that there isn't a single batch size suitable for all training runs. When the training set size is relatively large, a batch size of 1024 is used. This value was chosen as a batch size any smaller led to the overall training time becoming prohibitively long. As the size of the training set is reduced, this batch size eventually becomes unsuitably large in comparison to the dataset size; for example, a whole epoch of the smallest training set would fit into a single batch, and we would no longer be performing stochastic gradient descent. To address this, batch size is reduced for the smaller datasets by limiting it to a maximum of $\frac{1}{128}$ of the training set size.

A limitation of having batch size vary with training set length is that it becomes another potential explanation for differences in performance. We argue that this does not detract from the results as the batch sizes that are paired with each training set size are representative of what a practitioner would use; for example, it would not be representative of common practice to train a model on the 2^{25} length training sets with a batch size of 4.

Steps per evaluation. Models are evaluated every 1024 training steps, or every epoch, whichever is sooner. Evaluating every epoch is too infrequent for the larger training sets. The effect of these settings is still to evaluate more frequently for smaller datasets; this is suitable as models quickly overfit on these datasets, and it is desirable to have more frequent evaluations in order to select the best-performing model parameters.

Table 5: Relationship between training set size and a number of settings: batch size, number of epochs, number of steps and number of evaluations. Batch size is capped at $\frac{1}{128}$ of the training set size. The number of epochs is capped at 512. 2^{27} samples are drawn, or until the epoch limit of 512 is reached. An evaluation is run every epoch or every 1024 steps, whichever is sooner. A consequence of these settings is that all configurations share the same number of steps.

Train length	Batch size	Epochs	Steps	Evals
1024	8	512	65536	512
2048	16	512	65536	512
4096	32	512	65536	512
8192	64	512	65536	512
16384	128	512	65536	512
32768	256	512	65536	512
65536	512	512	65536	512
131072	1024	512	65536	512
262144	2048	512	65536	512
524288	2048	256	65536	256
1048576	2048	128	65536	128
2097152	2048	64	65536	64
4194304	2048	32	65536	64
8388608	2048	16	65536	64
16777216	2048	8	65536	64
33554432	2048	4	65536	64

Learning rate. With multiple datasets, models and batch sizes, fixing a single learning rate would risk skewing results in favour of configurations that best suit the chosen learning rate. Instead of fixing a learning rate, we fix a strategy for selecting a learning rate. This is described in the next section.

E.3 Learning rate selection

For all configurations of models and datasets, an individual maximum learning rate is chosen by using the learning rate range test introduced by Smith [2017]. An issue with this approach is its sensitivity to noise in the loss curve generated by a sweep over learning rates; this noise makes it difficult to identify the region of steepest descent. We modify the approach slightly in order to increase robustness: for each configuration we carry out 8 learning rate sweeps. Averaging 8 sweeps is insufficient to smooth out the noise in the loss curves. Instead, we use Kalman filtering to estimate the expected change in loss at each learning rate and integrate this curve to obtain the final smoothed loss curve. This process generates smooth curves from which critical points can be more easily identified. From the smoothed loss curve, we choose a learning rate that is the geometric mean between the point of steepest descent and the point where the loss curve ends or begins to increase. The selection of the two points—the point of steepest descent and the endpoint—is not always reliable, and so all selected learning rates were manually inspected, with a small number being manually overridden.

The results of this learning rate sweep for `gpt-a-cat` for the synthetic datasets are shown in Figure 24. The same results but for `rnn-nn` are shown in Figure 25. Interestingly, these results show that the learning rate identified by the range test varies very little between batch sizes on these datasets. To reduce the number of manual overrides, we take the median learning rate across batch sizes as the final learning rate and manually override this for configurations where it is too high or low.

Similar to the situation with batch size, having a learning rate vary across models and datasets introduces an extra factor that may account for differences in performance across configurations. This may be considered a limitation; however, we argue that to fairly compare models, training should be *best-effort*—that is, each model should be trained with the learning rate most appropriate for it and the dataset it is being trained on. In this sense, while the learning rate varies across models and datasets, the strategy for choosing the learning rate is held constant.

E.4 Compute resources

There were three computationally intensive steps for each experiment: learning rate sweeps, training and evaluation. Learning rate sweeps and model evaluation were carried out on a single workstation, with GPU, CPU and RAM specifications: Nvidia RTX 4090 GPU, AMD Ryzen Threadripper PRO 5975WX and 256 GiB RAM. Depending on the experiment, training was carried out on either this workstation or by using 10 Nvidia A40 GPUs from an internal cluster. The wall-clock durations for each of these three steps are reported below, separated by the sections where the results are used. The durations are affected by concurrent jobs that may have been sharing resources, and may include a tapering period where there is not enough remaining work to utilize all GPUs.

For the spike prediction experiment (Section 2), all three steps were run on the workstation. Time taken for the learning rate sweeps, training and evaluation was ~9 hours, ~122 hours and ~9 hours respectively. These times include the time taken to run the additional experiment using the distance function head that appeared in Appendix B. The learning rate sweeps for Sections 3 to 5 took ~20 hours. Training for the 10 repeats in Section 3 took ~227 hours on the workstation, and evaluation took ~1 hour. Training all models of the synthetic and “real-world” datasets (Section 4, Section 5 and the corresponding supplementary results) took ~223 hours on the cluster. Evaluation took ~11 hours on the workstation. For the modulo datasets (Section 6), the learning rate sweeps took ~16 hours on the workstation, training took ~167 hours on the cluster, and evaluation took ~7 hours on the workstation.

Across all experiments, learning rate sweeps took ~45 hours on the workstation, training took ~349 hours on the workstation and ~390 hours on the cluster, and evaluation took ~27 hours on the workstation. We estimate that exploratory, failed or unused experiments used approximately 3 times more compute, combined.

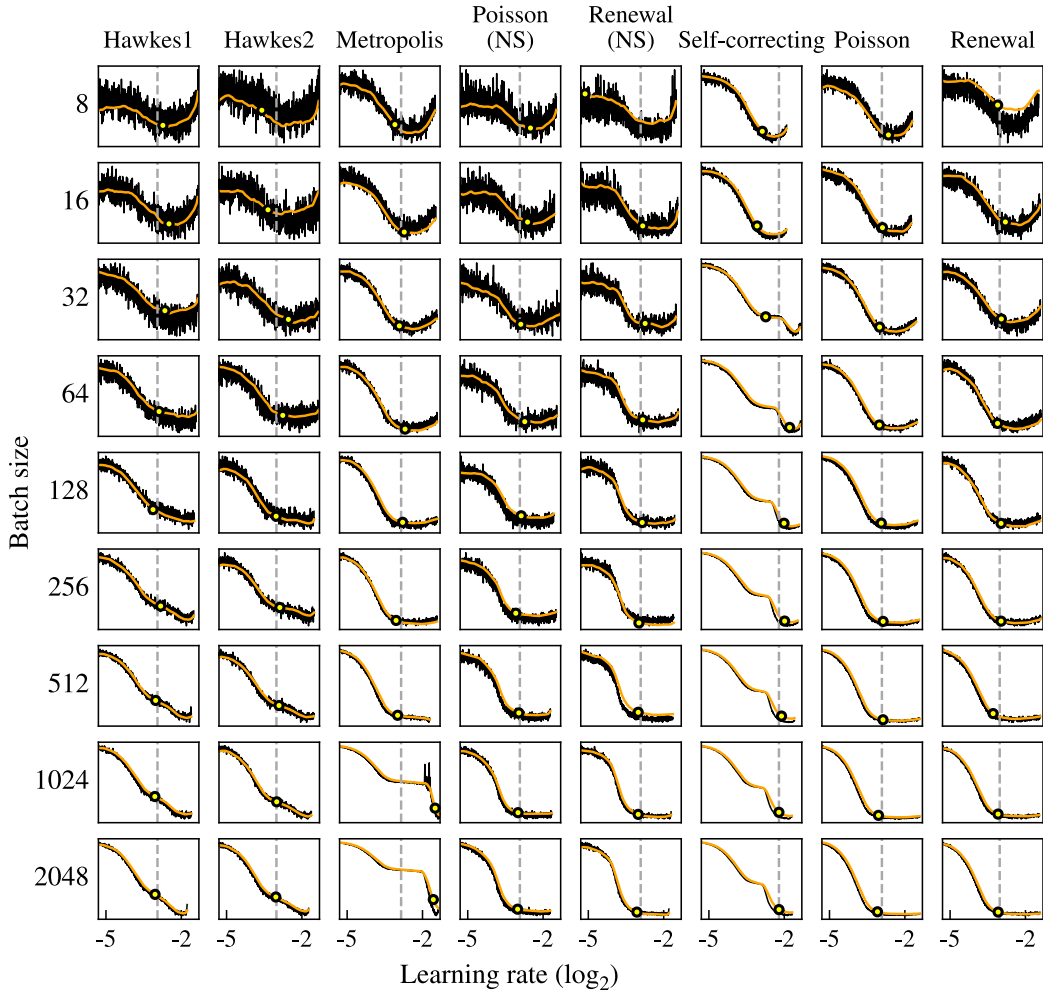


Figure 24: Learning rate sweep for `gpt-a-cat` for the synthetic datasets. The black trace (—) is the mean loss over 8 runs. The orange trace (—) is the Kalman smoothed loss. The yellow points (o) mark the geometric mean between the point of steepest descent and the point where the curve increases or ends—the proposed learning rate. The dashed vertical grey line marks the median proposed learning rate across batch sizes. As the proposed learning rate varies little between batch sizes, in this work, we choose the median learning rate across batch sizes to be used for all batch sizes. We manually select the learning rate for a configuration if the median learning rate is unsuitably high or low.

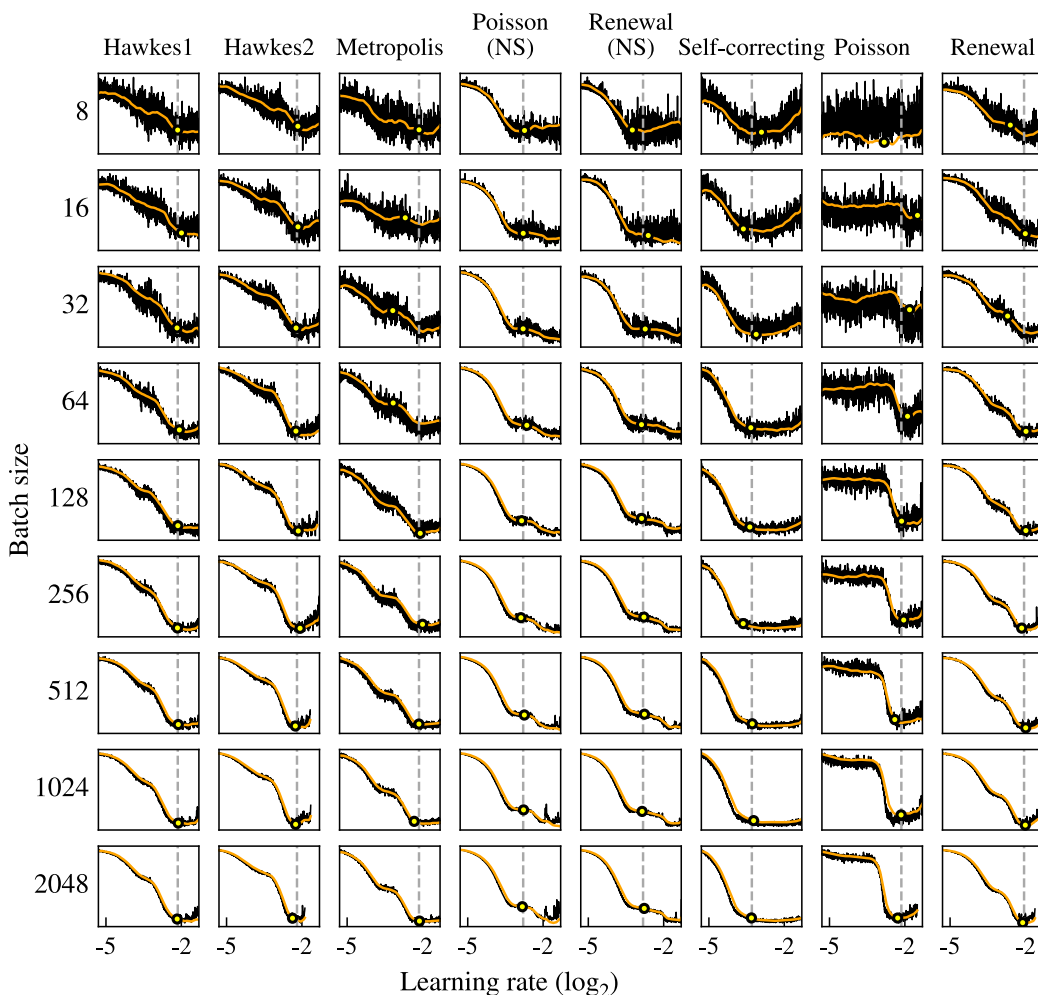


Figure 25: Learning rate sweep for `rnn-nn` for the synthetic datasets. The black trace (---) is the mean loss over 8 runs. The orange trace (---) is the Kalman smoothed loss. The yellow points (o) mark the geometric mean between the point of steepest descent and the point where the curve increases or ends—the proposed learning rate. The dashed vertical grey line marks the median proposed learning rate across batch sizes.

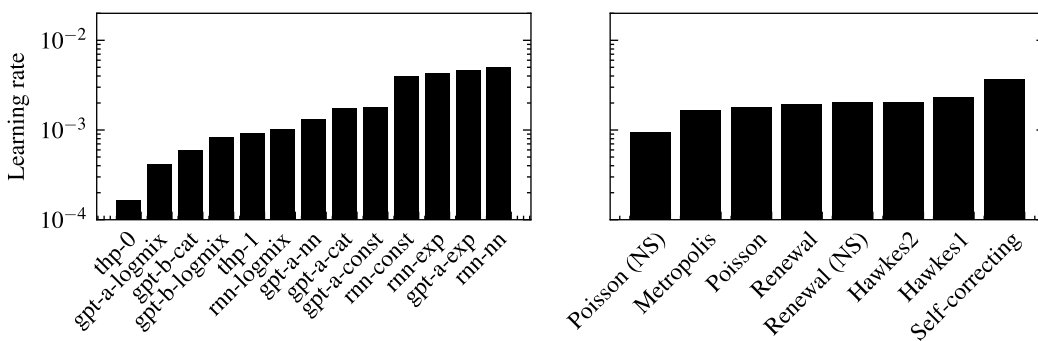


Figure 26: **Left:** mean learning rate used for each model (mean over synthetic datasets). **Right:** mean learning rate used for each of the synthetic datasets (mean over all models).